JOURNAL OF GEOPHYSICAL RESEARCH, VOL. 114, B06207, doi:10.1029/2008JB005852, 2009

Viscous constitutive relations of solid-liquid composites in terms of grain boundary contiguity: 3. Causes and consequences of viscous anisotropy

Yasuko Takei[1] and Benjamin K. Holtzman[2]

Received 5 June 2008; revised 24 February 2009; accepted 17 March 2009; published 25 June 2009.

[1] The viscous constitutive relations of partially molten rocks developed here show that an anisotropy in grain-scale melt distribution can lead to a strong anisotropy in the viscosity of the solid framework. With anisotropic viscosity, a direct coupling between shear and isotropic components of stress occurs, and hence, the role of shear deformation in melt migration significantly increases. We demonstrate the significant effects of viscous anisotropy on melt migration dynamics by solving the solid-liquid two-phase dynamics for two simple cases. First, in rotary shear deformation, an anisotropy creates a driving force for melt migration up stress gradients in the solid matrix, which does not exist with isotropic viscosity. Second, in uniform simple shear deformation, melt segregates spontaneously into low-angle bands due to anisotropic melt alignment, in close agreement with experimental observations. Our results indicate that stress-induced melt alignment at the grain scale drives further melt redistribution over distances much longer than the grain scale. The development of such ''multiscale anisotropy'' is demonstrated by ''forward'' or ab initio approaches based on the equations of two-phase dynamics, in which the viscous constitutive relation is based on observed microstructure and realistic rheology. When applied to a simple approximation of flow in the mantle beneath ridge and subduction zone, the anisotropic constitutive relation significantly affects melt migration patterns.

Citation: Takei, Y., and B. K. Holtzman (2009), Viscous constitutive relations of solid-liquid composites in terms of grain boundary contiguity: 3. Causes and consequences of viscous anisotropy, *J. Geophys. Res.*, *114*, B06207, doi:10.1029/2008JB005852.

1. Introduction

[2] It is well known that the Earth's upper mantle possesses significant elastic anisotropy. However, the presence of viscous anisotropy is not easily constrained and its importance is not well understood. Previous studies on the effects of viscous anisotropy on geodynamics showed that viscous anisotropy can significantly affect patterns and length scales of mantle convection and postglacial rebound [*Saito and Abe*, 1984; *Honda*, 1986; *Christensen*, 1987; *Lev and Hager*, 2008]. These studies attributed anisotropy mostly to solid state rock fabrics and considered incompressible fluid dynamics. Our concern in this paper is the viscous anisotropy of partially molten rocks. One of the important implications of the first of our companion papers [*Takei and Holtzman*, 2009a] (hereinafter referred to as TH1) is that an anisotropy in grain-scale melt distribution can lead to a strong anisotropy in the viscosity of the solid framework. The essential difference from previous studies is that we consider the dynamics of solid-liquid two-phase systems in which local compaction and decompaction of the solid framework occur, coupled to liquid migration. In this paper, we demonstrate the significant consequences of viscous anisotropy on the dynamics of partially molten rocks.

[3] Shear deformation of partially molten rocks is considered to play important roles in segregation of melt from the mantle. These interactions have been studied over wide length scales, ranging from plate boundary scale to laboratory sample scale. At the plate boundary scale, detailed theoretical studies on the liquid pressure gradients induced by mantle flow were performed for mid-ocean ridge and subduction zone settings [*Spiegelman and McKenzie*, 1987; *Phipps Morgan*, 1987]. In both settings, mantle shear deformation drives horizontal migration and focusing of melt toward the singular point in the flow field. This result is important as a possible explanation for narrow zone of volcanism and broad zone of melt production at mid-ocean ridge. In the partially molten rock samples experimentally deformed in simple shear, spontaneous segregation of melt into low-angle bands was observed [*Holtzman et al.*, 2003a, 2003b, 2005; *Holtzman and Kohlstedt*, 2007]. This result is important as a possible mechanism for the development of high-permeability pathways, which are required to explain the rapid ascent of melt indicated from the significant radioactive disequilibrium in young basalts [e.g., *Kelemen*

[1]Earthquake Research Institute, University of Tokyo, Tokyo, Japan.
[2]Lamont-Doherty Earth Observatory, Earth Institute at Columbia University, Palisades, New York, USA.

0148-0227/09/2008JB005852$09.00

et al., 1997; *Spiegelman et al.*, 2001; *Iwamori*, 1994]. Such rapid ascent cannot be explained by the low permeability of an isotropic network of grain edge melt tubules which develop under hydrostatic stress.

[4] In modeling the effects of shear deformation on melt migration, viscous rheology of partially molten rocks plays an essential role. In the focusing of melt driven by mantle flow, a key parameter determining the intensity of the focusing is the shear viscosity of the solid matrix. Also, in the spontaneous segregation of melt into melt-rich bands, porosity-weakening viscosity plays an important role [*Stevenson*, 1989]. Although the observed low angle of the bands cannot be explained by the simple model with porosity-weakening viscosity [*Spiegelman*, 2003], a model extended to nonlinear rheology can explain the low angle due to the balance of porosity weakening and strain rate weakening [*Katz et al.*, 2006]. However, until now, the effects of shear deformation have been explored only for systems with isotropic viscosities. Although grain-scale melt alignment, which causes large viscous anisotropy, was observed simultaneously with the melt-rich networks of channels [*Holtzman and Kohlstedt*, 2007], relations between the two observations have not been explored.

[5] This study is the first attempt to investigate the effects of matrix shear deformation on melt migration with anisotropic viscosities. Because viscous anisotropy causes a direct coupling between shear and isotropic components, the roles of shear deformation in melt migration are significantly increased. We demonstrate the occurrence of melt migration up stress gradients in the solid framework, which does not occur in systems with isotropic viscosity, and also the spontaneous segregation of melt into low-angle bands, consistent with experimental observation. Our results show that the viscous anisotropy resulted from the melt alignment at the grain scale drives further melt redistribution over distances greater than the grain scale. In other words, development and consequences of ''multiscale'' structures are predicted, in which the grain size and compaction length provide two important reference scales.

[6] In sections 2–7, we first introduce the tensor representation of anisotropic viscosity of solid-liquid two-phase system (section 2). We present a simple 2-D microstructural model and derive viscous constitutive relations as functions of grain-scale contact geometry (section 3). Then, by combining the anisotropic viscous constitutive relation with mass and momentum conservation of the solid-liquid two-phase system (section 4), we solve the melt migration under a rotary shear deformation (section 5) and under a simple shear deformation (section 6). To illustrate potential implications for geodynamics, we present approximate solutions for melt migration in the mantle beneath mid-ocean ridges and subduction zones (section 7). The approaches developed in this paper are ''forward'' or ab initio approaches based on the equations of solid-liquid two-phase dynamics, in which the viscous constitutive relations bridge microscopic and macroscopic processes. These forward models complement the inverse approaches discussed by TH1.

2. Tensor Representation of Anisotropic Viscosity

[7] We consider a solid-liquid two-phase system in which the solid matrix deforms by grain boundary diffusion creep. Anisotropy in matrix viscosity can be generally represented in terms of the viscosity tensor C_{ijkl} as

$$\sigma_{ij}^S - P^l \delta_{ij} = C_{ijkl} \dot{\varepsilon}_{kl}^f \tag{1}$$

or

$$\sigma_{ij}^B - P^l \delta_{ij} = C_{ijkl}^B \dot{\varepsilon}_{kl}^f, \tag{2}$$

where σ_{ij}^S is solid stress (tension positive), P^l is liquid stress (tension positive), σ_{ij}^B is the bulk (or total) stress defined by

$$\sigma_{ij}^B = (1-\phi)\sigma_{ij}^S + \phi P^l \delta_{ij} \tag{3}$$

with melt fraction ϕ, and $\dot{\varepsilon}_{ij}^f$ represents framework strain rate which is defined by the macroscopic (average) velocity field of the solid phase, $\mathbf{v}^S$, as

$$\dot{\varepsilon}_{ij}^f = \frac{1}{2}\left(\frac{\partial v_i^S}{\partial x_j} + \frac{\partial v_j^S}{\partial x_i}\right). \tag{4}$$

Even if the constituent materials are incompressible, the volumetric component of the framework strain rate, $\dot{\varepsilon}_{ii}^f$, can be nonzero due to the occurrence of compaction/decompaction. C_{ijkl} in equation (1) and C_{ijkl}^B in equation (2) are simply related by $C_{ijkl}^B = (1-\phi)C_{ijkl}$.

[8] In the first of the companion papers (TH1), a theoretical framework to derive viscous constitutive relations of partially molten rocks deforming within the regime of grain boundary diffusion creep was developed on the basis of the grain-scale model (contiguity model). In section 3, by applying this theory to a 2-D grain model, the viscosity tensor is derived as a function of grain-to-grain contact geometry described by the contact function X^C. Then, by constraining the contact geometry with experimental observations, anisotropic viscosities of partially molten rocks are predicted. Therefore, section 3 provides an important foundation for the anisotropic viscosity used in sections 4–7. However, readers who are mostly interested in the macroscopic consequences or phenomenological aspects of the viscous anisotropy may leap to section 4 and refer to section 3 as needed.

3. Viscosity Tensor in 2-D Based on Contiguity Model

[9] We consider a solid-liquid composite system, in which the contact state of each grain with neighboring grains is described by a contact function X^C defined on the grain surface. X^C takes a value of 1 on the contact surface and 0 on the pore surface. For simplicity, we consider a 2-D grain with 8 contact faces or patches (Figure 1);

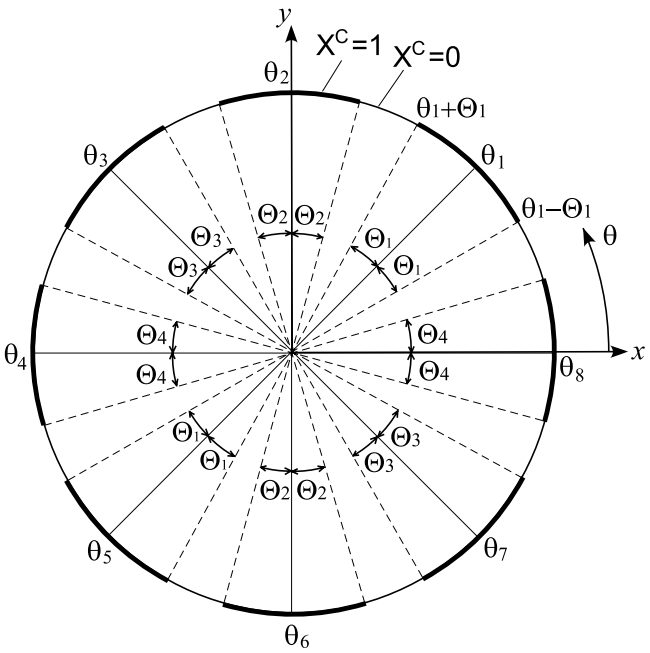

Figure 1. A two-dimensional grain with 8 contact patches in the directions of $\theta_k = k\pi/4$ ($k = 1$–8). The contact function $X^C(\theta)$ takes a value of 1 on the contact patches (thick line segments) and 0 on the pore surface (thin line segments). The patch size is given by angle $2\Theta_k$, where point symmetry given by $\Theta_{k+4} = \Theta_k$ ($k = 1$–4) is assumed.

X^C takes a value of 1 on the 8 contact patches placed at $\theta_k - \Theta_k \le \theta \le \theta_k + \Theta_k$ ($k = 1, 2, .., 8$) and 0 on the pore surface at $\theta_k + \Theta_k \le \theta \le \theta_{k+1} - \Theta_{k+1}$, where $\theta_k = k\pi/4$ represents the center of the kth contact patch and $2\Theta_k$ represents the patch size. A point symmetry, $\Theta_1 = \Theta_5$, $\Theta_2 = \Theta_6$, $\Theta_3 = \Theta_7$, and $\Theta_4 = \Theta_8$, is assumed. Using the theory developed by TH1, the viscous constitutive relation of the composite can be derived in an analytical form as

$$\begin{pmatrix} \dfrac{\left(\sigma^B_{xx} - P^l\right) + \left(\sigma^B_{yy} - P^l\right)}{2} \\ \dfrac{\left(\sigma^B_{xx} - P^l\right) - \left(\sigma^B_{yy} - P^l\right)}{2} \\ \sigma^B_{xy} \end{pmatrix} = \begin{pmatrix} \xi & \zeta_2 & \zeta_3 \\ \zeta_2 & \eta + \zeta_1 & 0 \\ \zeta_3 & 0 & \eta - \zeta_1 \end{pmatrix} \cdot \begin{pmatrix} \dot{\varepsilon}^f_{xx} + \dot{\varepsilon}^f_{yy} \\ \dot{\varepsilon}^f_{xx} - \dot{\varepsilon}^f_{yy} \\ 2\dot{\varepsilon}^f_{xy} \end{pmatrix}, \tag{5}$$

where ξ and η represent the generalized forms of bulk and shear viscosities defined by

$$\begin{cases} \xi = \dfrac{(1-\phi)\eta_{cc}}{\pi} \dfrac{2}{3} \displaystyle\sum_{k=1}^{4} (2\Theta_k)^3 \\ \eta = \dfrac{(1-\phi)\eta_{cc}}{\pi} \left(\displaystyle\sum_{k=1}^{4} 2\Theta_k - \sum_{k=1}^{4} \frac{1}{2\Theta_k} \sin^2(2\Theta_k) \right), \end{cases} \tag{6}$$

ζ_1, ζ_2, and ζ_3 are anisotropy components defined by

$$\begin{cases} \zeta_1 = \dfrac{(1-\phi)\eta_{cc}}{2\pi} \Big(\sin(4\Theta_1) - \sin(4\Theta_2) + \sin(4\Theta_3) \\ \quad - \sin(4\Theta_4) - \dfrac{1}{\Theta_1} \sin^2(2\Theta_1) + \dfrac{1}{\Theta_2} \sin^2(2\Theta_2) \\ \quad - \dfrac{1}{\Theta_3} \sin^2(2\Theta_3) + \dfrac{1}{\Theta_4} \sin^2(2\Theta_4) \Big), \\ \zeta_2 = \dfrac{(1-\phi)\eta_{cc}}{\pi} (4\Theta_2 \cos(2\Theta_2) - 2\sin(2\Theta_2) \\ \quad - 4\Theta_4 \cos(2\Theta_4) + 2\sin(2\Theta_4)), \\ \zeta_3 = \dfrac{(1-\phi)\eta_{cc}}{\pi} (-4\Theta_1 \cos(2\Theta_1) + 2\sin(2\Theta_1) \\ \quad + 4\Theta_3 \cos(2\Theta_3) - 2\sin(2\Theta_3)), \end{cases} \tag{7}$$

and η_{cc} represents the Coble creep viscosity in two dimensions, which is explicitly given by equation (36) of TH1. The derivation is based on the calculation of the radial component of traction f_r on the surface of each grain under a given macroscopic strain rate $\dot{\varepsilon}^f_{ij}$ and liquid stress P^l, where tangential components of the traction are assumed to be zero (TH1). For later use, the explicit form of f_r is written here: on the kth contact patch,

$$\begin{aligned} \frac{f_r - P^l}{2\eta_{cc}} = & -2\left(\dot{\varepsilon}^f_{xx} + \dot{\varepsilon}^f_{yy}\right)(\theta - \theta_k - \Theta_k)(\theta - \theta_k + \Theta_k) \\ & + \left(\dot{\varepsilon}^f_{xx} - \dot{\varepsilon}^f_{yy}\right)\Big(\cos(2\theta) - \cos(2\theta_k)\cos(2\Theta_k) \\ & + \frac{\theta - \theta_k}{\Theta_k} \sin(2\theta_k)\sin(2\Theta_k) \Big) + 2\dot{\varepsilon}^f_{xy}\Big(\sin(2\theta) \\ & - \sin(2\theta_k)\cos(2\Theta_k) - \frac{\theta - \theta_k}{\Theta_k} \cos(2\theta_k)\sin(2\Theta_k) \Big), \end{aligned} \tag{8}$$

and on the pore surface, $f_r = P^l$ or $f_r - P^l = 0$. (To derive equations (5)–(7), f_r is first calculated from equations (21) and (26)–(28) of TH1, and then the weighted average of f_r over the grain surface is calculated from equation (34) of TH1 to obtain the relationship between macroscopic stresses, σ^S_{ij} and P^l, and strain rate, $\dot{\varepsilon}^f_{ij}$.)

[10] Equation (5) can be rewritten as

$$\begin{pmatrix} \sigma^B_{xx} - P^l \\ \sigma^B_{yy} - P^l \\ \sigma^B_{xy} \\ \sigma^B_{yx} \end{pmatrix} = \begin{pmatrix} \xi + (\eta + \zeta_1) + 2\zeta_2 & \xi - (\eta + \zeta_1) - 2\zeta_2 & \zeta_3 & \zeta_3 \\ \xi - (\eta + \zeta_1) & \xi + (\eta + \zeta_1) & \zeta_3 & \zeta_3 \\ \zeta_3 & \zeta_3 & \eta - \zeta_1 & \eta - \zeta_1 \\ \zeta_3 & \zeta_3 & \eta - \zeta_1 & \eta - \zeta_1 \end{pmatrix} \begin{pmatrix} \dot{\varepsilon}^f_{xx} \\ \dot{\varepsilon}^f_{yy} \\ \dot{\varepsilon}^f_{xy} \\ \dot{\varepsilon}^f_{yx} \end{pmatrix}, \tag{9}$$

which gives the explicit form of the viscous constitutive relation (2) in two dimensions. Viscosity tensor C^B_{ijkl} ($i, j, k, l = x, y$) is symmetric for the exchanges of i and j, k and l, and ij and kl, and hence generally consists of 6 independent components. The viscosity tensor C^B_{ijkl} derived here has four degrees of freedom, corresponding to the 4 parameters $\Theta_1 - \Theta_4$, which is smaller than 6. However, as shown below,

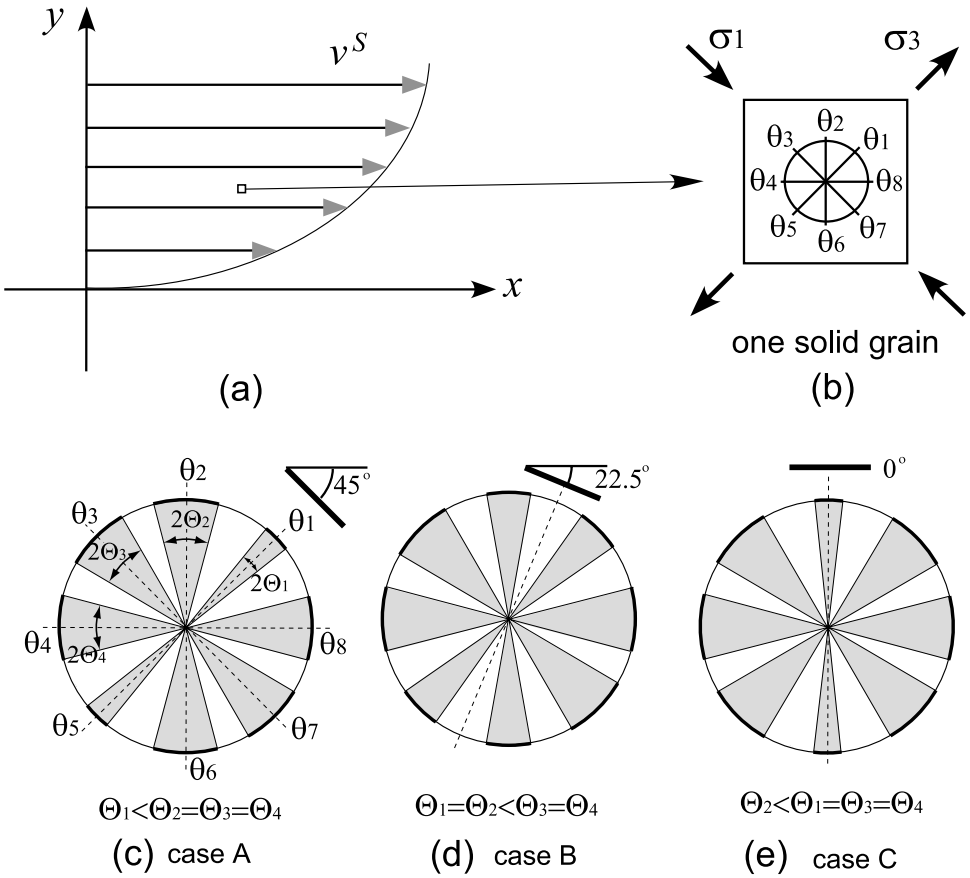

Figure 2. (a) Two-dimensional Cartesian coordinate axes (x, y) and (b) grain coordinate system θ_k (k = 1–8). The angles $\theta_{1,5}$ and $\theta_{3,7}$ coincide with the directions of σ_3 and σ_1, respectively, for a simple shear described by velocity gradient $v_{x,y}{}^S$ (>0). (c, d, e) Three types of stress-induced anisotropy defined under the principal stress direction shown in Figures 2a and 2b. In case A, Θ_1 is reduced; in case B, Θ_1 and Θ_2 are reduced; in case C, Θ_2 is reduced. Direction of melt alignment corresponding to each contact anisotropy is shown with the angle to the shear plane.

these 4 parameters are sufficient for describing various contact anisotropies reported from experimental studies.

[11] Previous studies on the effects of viscous anisotropy on geodynamics were performed on incompressible fluid flow. For comparison, anisotropic viscosity in two dimensions for incompressible flow is presented in Appendix A. The difference between equation (9) and equation (A1) shows the essential difference between the previous studies on incompressible flow and the present study on compressible flow of the solid framework.

3.1. Isotropic Viscosity

[12] Under hydrostatic stress, equilibrium texture develops at which the interfacial energy is at a minimum. The equilibrium texture is isotropic and is represented by $\Theta_1 = \Theta_2 = \Theta_3 = \Theta_4$. In this case, $\zeta_1 = \zeta_2 = \zeta_3 = 0$ and viscosity tensor in equation (9) becomes an isotropic tensor:

$$\begin{pmatrix} \sigma^B_{xx} - P^l \\ \sigma^B_{yy} - P^l \\ \sigma^B_{xy} \\ \sigma^B_{yx} \end{pmatrix} = \begin{pmatrix} \xi+\eta & \xi-\eta & 0 & 0 \\ \xi-\eta & \xi+\eta & 0 & 0 \\ 0 & 0 & \eta & \eta \\ 0 & 0 & \eta & \eta \end{pmatrix} \begin{pmatrix} \dot{\varepsilon}^f_{xx} \\ \dot{\varepsilon}^f_{yy} \\ \dot{\varepsilon}^f_{xy} \\ \dot{\varepsilon}^f_{yx} \end{pmatrix}. \quad (10)$$

In section 3.4, Θ_i (i = 1–4) of the equilibrium texture is related to melt fraction and dihedral angle.

3.2. Stress-Induced Anisotropy

[13] We consider the microstructural anisotropies observed in the experimentally deformed partially molten rocks or rock analogue. Our discussions focus on stress-induced anisotropy, in which the direction and amplitude of the anisotropy are determined by stress. In the applications presented in sections 5 and 6, we consider simple shear deformation in which the principal stress axes are fixed with respect to the spatial coordinate system. Hence, the direction of anisotropy can be fixed with respect to the spatial coordinate system. Here, σ_1 (largest compressive stress) and σ_3 (least compressive stress) directions are taken to be (x, y) = (−1, 1) and (x, y) = (1, 1), respectively (Figures 2a and 2b). In other words, we consider a stress field given by σ^B_{xy}(>0). Directions of the 8 contact patches θ_k (k = 1–8) for each grain can also be fixed to the spatial coordinate system (Figure 2b).

3.2.1. Case A

[14] The development of stress-induced anisotropy was reported for partially molten rock analogue under nearly pure shear deformation [*Takei*, 2005; also Stress-induced

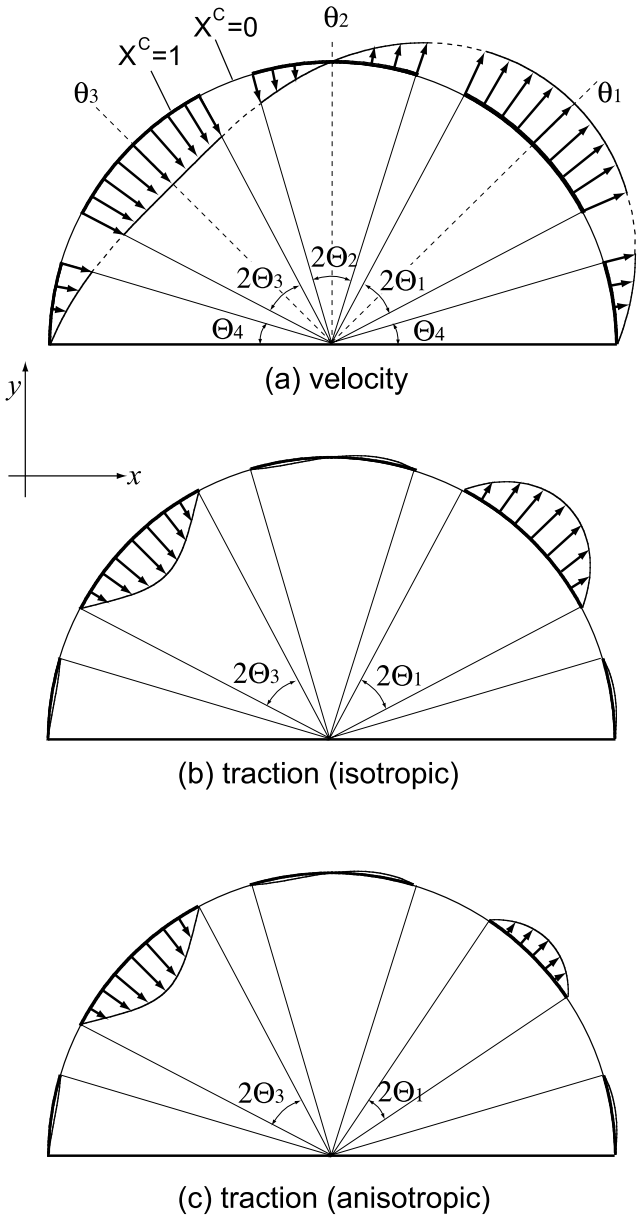

Figure 3. Microscopic mechanism for coupling between shear and isotropic components. (a) Velocity distribution at the grain-to-grain contact faces ($X^C = 1$, thick line segments) required under a given macroscopic strain rate $\dot{\varepsilon}_{xy}^f$. At the pore surface ($X^C = 0$, thin line segments), not velocity but traction condition ($f_r - P^l = 0$) is required. (b, c) Differential traction $f_r - P^l$ for isotropic contact geometry (Figure 3b) and for anisotropic contact geometry (Figure 3c) of case A. Under isotropic contact geometry, the differential traction is symmetric between the compressive and tensile directions and does not produce isotropic effective stress. Under case A anisotropic contact geometry, the differential traction is reduced in the tensile direction, producing compressive effective stress.

anisotropy of partially molten rock analogue deformed under quasi-static loading test, submitted to *Journal of Geophysical Research*, 2009]. In this experiment, melt segregation over distances greater than the grain scale did not occur, and hence the measured mechanical anisotropy can be attributed to grain-scale contact anisotropy. Microstructure under stress, which was monitored in situ using ultrasonic shear waves, showed that the area of the contact faces whose normals are nearly parallel to the σ_3 direction decreases, whereas the areas of the other contact faces do not change. Under the direction of stress shown in Figures 2a and 2b, this anisotropy can be represented by reducing Θ_1 such that $\Theta_1 < \Theta_2 = \Theta_3 = \Theta_4$, which is hereafter referred to as case A (Figure 2c). In this case, ζ_2 in equation (9) is always zero. Under conditions of simple shear, case A anisotropy represents a melt alignment oriented at an angle of 45° to the shear plane (Figure 2c).

3.2.2. Cases B and A′

[15] In partially molten rocks deformed to more than 200% strain under simple shear, the alignment of melt subparallel to the shear plane has been reported by *Zimmerman et al.* [1999] and *Holtzman and Kohlstedt* [2007]. Although *Holtzman and Kohlstedt* [2007] reported not only the grain-scale melt alignment but also the melt segregation over distances greater than the grain scale, we focus only on the grain-scale geometry in this section. On the basis of their observation that the long axes of the melt pockets are oriented predominantly at an angle of 20° from σ_1 [*Zimmerman et al.*, 1999], we approximate this anisotropy by reducing Θ_1 and Θ_2 such that $\Theta_1 = \Theta_2 < \Theta_3 = \Theta_4$, which is hereafter referred to as case B (Figure 2d). In this case, ζ_1 in equation (9) is always zero. Intermediate cases between A and B described by $\Theta_1 < \Theta_2 < \Theta_3 = \Theta_4$ is referred to as case A′.

3.2.3. Case C

[16] For comparison, we further consider the case in which the melt alignment is parallel to the shear plane. This geometry, represented by reducing Θ_2 such that $\Theta_2 < \Theta_1 = \Theta_3 = \Theta_4$, is referred to as case C (Figure 2e). In this case, ζ_3 in equation (9) is always zero.

3.3. Coupling Between Shear and Isotropic Components

[17] Under the stress orientation shown in Figure 2a, the major component of the strain rate tensor is $\dot{\varepsilon}_{xy}^f$ (= $\dot{\varepsilon}_{yx}^f$). Equation (5) shows that ζ_3 defines the coupling between the shear component $\dot{\varepsilon}_{xy}^f$ and the isotropic component of the effective stress, $(\sigma_{xx}^B + \sigma_{yy}^B)/2 - P^l$. When $\zeta_3 \neq 0$, the shear strain rate $\dot{\varepsilon}_{xy}^f$ contributes the component $2\zeta_3\dot{\varepsilon}_{xy}^f$ to the isotropic stress component, which does not occur with isotropic viscosity. Significant consequences of this coupling in melt migration dynamics are shown in sections 5–7. Here, we discuss the microscopic mechanism and define the coupling factor γ.

[18] The microscopic mechanism of the coupling between the shear and isotropic components is illustrated in Figure 3. The macroscopic strain rate $\dot{\varepsilon}_{xy}^f$ causes the radial velocity field on the grain as shown in Figure 3a. The radial traction on the contact patches, satisfying this velocity condition at $X^C = 1$ and traction condition $f_r = P^l$ at $X^C = 0$, is given by equation (8). The resulting differential traction $f_r - P^l$ is shown in Figure 3b for isotropic contact geometry and in Figure 3c for anisotropic contact geometry of case A. When the contact geometry is isotropic ($\Theta_1 = \Theta_3$), velocity and differential traction on the contact patches in the tensile and compressive directions (θ_1 and θ_3, respectively) are equal in

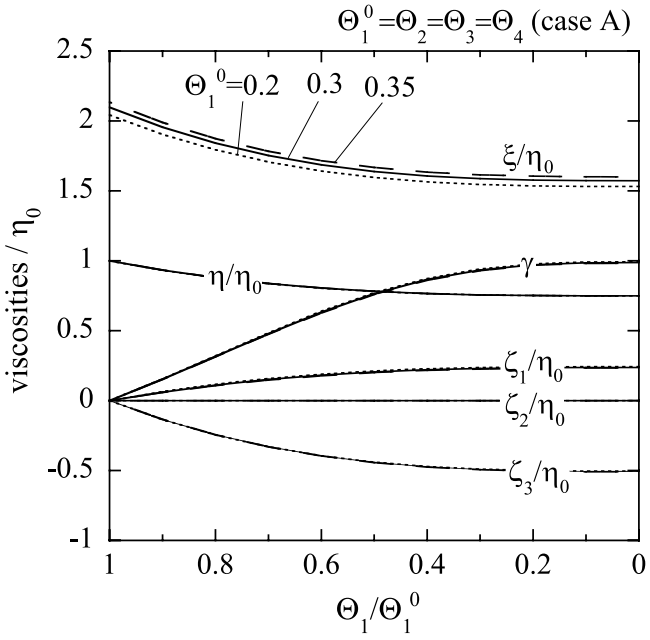

Figure 4. For anisotropic contact geometry of case A, viscosity components ξ, η, ζ_1, ζ_2 and ζ_3 normalized to isotropic viscosity η_0(= $\eta(\Theta_1 = \Theta_1^0)$) and nondimensional coupling factor γ defined by equation (11) are shown as functions of the size of the reduced patch Θ_1 normalized to the initial size Θ_1^0(= 0.2, 0.3, 0.35).

amplitude and opposite in sign, so no isotropic effective stress is produced (Figure 3b). When the contact geometry is anisotropic ($\Theta_1 < \Theta_3$), the amplitude of the differential traction needed to produce the same radial velocity is much smaller in the tensile direction (θ_1) because of the smaller patch size, producing an isotropic effective stress (Figure 3c). Because the reduction in the amplitude of differential traction occurs in the tensile direction, the resulting stress is compressive (negative). This is why ζ_3 is negative for case A, as discussed in section 3.4.

[19] We define a nondimensional coupling factor γ as the ratio between effective pressure and shear stress produced by shear deformation. From equation (9), when shear deformation is given by $\dot{\varepsilon}^f_{xy}$ and $\dot{\varepsilon}^f_{yx}$ components, γ is equal to the ratio of the off-diagonal components C^B_{xxij} and C^B_{yyij} ($i \neq j$) to the shear components C^B_{ijij} and C^B_{ijji} ($i \neq j$), as

$$\gamma = \left.\frac{-\left\{\left(\sigma^B_{xx}+\sigma^B_{yy}\right)/2 - P^l\right\}}{\sigma^B_{xy}}\right|_{\text{by } \dot{\varepsilon}^f_{xy} \text{ and } \dot{\varepsilon}^f_{yx}} = -\frac{\zeta_3}{\eta-\zeta_1}. \quad (11)$$

When $\sigma^B_{xy} > 0$, ζ_3 takes a negative value and hence γ takes a positive value, as discussed in section 3.4. (When $\sigma^B_{xy} < 0$, ζ_3 is positive and γ is negative for case A.)

[20] The coupling between shear and isotropic components was actually observed in the deformation experiments on partially molten rock analogue, in which the contact anisotropy of case A developed [*Takei*, 2001, 2005, Figure 2, also submitted manuscript, 2009]. The compressive effective stress was produced by shear deformation, confirming the validity of the present model result.

[21] In Figure 3 and in those experiments, the coupling between shear and isotropic components is manifested in variations in the isotropic effective stress during uniform shear deformation without matrix compaction/decompaction (Figure 3a). However, the detailed consequences of the coupling differ depending on the boundary conditions of the system at hand. Under the boundary conditions considered in sections 5 and 6, matrix compaction/decompaction and/or liquid pressure gradients result from the coupling and drive melt migration.

3.4. Calculation of Viscosity Tensor Components

[22] We consider partially molten rocks with a given melt fraction and with various degrees of case A contact anisotropy. This situation can be modeled by gradually decreasing Θ_1 from Θ_1^0 to 0, while fixing Θ_2, Θ_3, and Θ_4 to equal Θ_1^0. The isotropic contact geometry obtained at $\Theta_1 = \Theta_1^0$ corresponds to the equilibrium geometry. Therefore, under a given dihedral angle, Θ_1^0 is determined by melt fraction ϕ. For texturally equilibrated partially molten rocks (dihedral angle ~20–30°), Θ_1^0 in the 2-D model can be roughly related to ϕ as $(8\Theta_1^0/\pi)^2 = 1 - A\phi^{\frac{1}{2}}$ with $A = 2$–2.3 (section 3.1 of *Takei and Holtzman* [2009b] (hereinafter referred to as TH2)). Therefore, Θ_1^0 = 0.2, 0.3, and 0.35, for example, roughly correspond to ϕ = 0.14–0.10, 0.043–0.033, and 0.01–0.008, respectively.

[23] Let η_0 equal η for the isotropic geometry with $\Theta_1 = \Theta_1^0$. For Θ_1^0 = 0.2, 0.3, and 0.35, the viscosity components ξ, η, ζ_1, ζ_2, and ζ_3 normalized to η_0 are shown in Figure 4 as functions of Θ_1 normalized to Θ_1^0. Also shown is γ defined by equation (11). It is demonstrated that the viscosity components normalized to η_0 are determined by Θ_1/Θ_1^0 independently of Θ_1^0. In other words, each viscosity component can be written as $\eta_0(\Theta_1^0)f(\Theta_1/\Theta_1^0)$ or $\eta_0(\phi)f(\Theta_1/\Theta_1^0)$ by using an arbitrary function f.

[24] In the applications considered in the latter part of this paper, we need to know the dependence of γ on shear stress amplitude (section 5) and also the dependences of $\eta - \zeta_1$ and ζ_3 on ϕ (section 6). We roughly estimate these dependences on the basis of the existing data and the present model results (sections 3.4.1 and 3.4.2). Validity and uncertainty of the estimation are further discussed in section 3.5.

3.4.1. Effect of Shear Stress Magnitude on Viscous Anisotropy

[25] On the basis of considerations of experimental observations and theory, we propose a relationship between stress amplitude and anisotropy amplitude. In deformation experiments on the partially molten rock analogue with constant ϕ, amplitude of the stress-induced anisotropy monitored by ultrasonic shear wave anisotropy was approximately linearly dependent on the shear stress amplitude (Y. Takei, submitted manuscript, 2009). Because elastic anisotropy is nearly proportional to contact anisotropy in theory (Figure 10c of TH1 and Figure 7b of *Takei* [1998]), the amplitude of contact anisotropy is inferred to be nearly proportional to the shear stress amplitude in the experiments. In the model presented here (Figure 4), viscosities and γ are linearly dependent on Θ_1 at small anisotropy ($\Theta_1 \simeq \Theta_1^0$) but become constant at large anisotropy ($\Theta_1 \simeq 0$). From an isotropic stress state and no anisotropy, we consider

that amplitude of anisotropy initially increases linearly with increasing stress, until a saturation limit above which the anisotropy is constant with increasing stress (also not considering structural causes of anisotropy at length scales longer than the grain size). We introduce the term "stress-saturated anisotropy" to refer to this state in which the anisotropy has become independent of the stress magnitude. The homologous stress (shear stress/rigidity) in the experiments was as small as 2.3×10^{-5}, presumably below this saturation threshold. In section 5, we assume that the stress amplitude is larger than the saturation value, so that viscosities and γ are assumed to be constant.

3.4.2. Effect of Melt Fraction on Viscosity and Its Anisotropy

[26] To estimate the dependence of each viscosity component on ϕ, now written as $\eta_0(\phi)f(\Theta_1/\Theta_1^0)$ with a known function f, we have to know the dependences of isotropic viscosity η_0 and normalized anisotropy factor Θ_1/Θ_1^0 on ϕ. In TH1, the present model developed for the 3-D isotropic geometry was shown to predict the porosity-weakening viscosity consistent with the empirical relationship $\eta \propto e^{-\lambda\phi}$, where $\lambda \simeq 25$ (Figure 11b of TH1). Hence, η_0 can be written as $\eta_0 = c\eta_{cc}e^{-\lambda\phi}$, where constant c was derived from our model as $\sim$0.2 (TH1). There is little theory or data that can constrain directly the dependence of Θ_1/Θ_1^0 on ϕ. The simplest assumption suitable for the first step is that compared to the strong porosity-weakening effect described by $\eta_0(\phi) \propto e^{-\lambda\phi}$, the effect of ϕ on the normalized anisotropy factor Θ_1/Θ_1^0 is minor and can be neglected. Under this assumption, two factors λ_η and λ_ζ representing the dependences of $\eta - \zeta_1$ and ζ_3, respectively, on ϕ under constant shear stress,

$$\begin{cases} \lambda_\eta = -\dfrac{\partial \ln(\eta - \zeta_1)}{\partial \phi} & (>0) \\ \lambda_\zeta = -\dfrac{\partial \ln \zeta_3}{\partial \phi} & (>0), \end{cases} \tag{12}$$

can be both simply approximated by the porosity weakening factor; $\lambda_\eta \simeq \lambda_\zeta \simeq \lambda$. These factors are used in section 6.

3.5. Predictions From Compositional Model

[27] Although stress induced anisotropy is observed in a wide range of experiments [*Daines and Kohlstedt*, 1997; *Zimmerman et al.*, 1999; *Takei*, 2001, 2005, also submitted manuscript, 2009], the underlying mechanisms are poorly understood. Therefore, in this study, the grain-scale anisotropy is constrained by experimental observations, while an understanding of the physical mechanisms is in development. In the compositional model developed by TH2, kinetic processes for viscosity and microstructural evolution are treated self-consistently, resulting in a mechanism for producing stress-induced anisotropy. The predicted direction of anisotropy is consistent with case A (Figure 7 of TH2) and the magnitude is a function of stress (and ϕ) (Figure 8b of TH2), consistent with the assumptions made in this study. The model also predicts the existence of stress-saturated anisotropy and its occurrence in the upper mantle (Figure 8b of TH2). The anisotropy of case A introduced in section 3.2.1 reduces total contiguity, $\varphi_{2D} = \sum_{k=1}^{4} 2\Theta_k/\pi$. However, the model predicts that both reduction and increase in contiguity occur in the σ_3 and σ_1 directions, respectively (Figure 7 of TH2), causing a slight increase in φ_{2D}. As stated by TH2, our understanding of microstructural process is not enough to theoretically predict the detailed behavior of the total contiguity under stress. Even if the anisotropy of case A is defined as $\Theta_1 < \Theta_2 = \Theta_4 < \Theta_3$, such that φ_{2D} is conserved, for example, formulations and qualitative aspects of this study are not significantly different. However, future progress in understanding microstructural processes under stress may improve the quantitative aspects of this study.

4. Applications to Melt Migration Dynamics

[28] In sections 5 and 6, two models are developed to illustrate the fundamental influence that anisotropic constitutive relations have on melt migration dynamics at scales much longer than the grain scale. The general continuum equations that describe coupling between melt migration and deformation are solved. These equations are composed of conservation of mass and momentum in a solid-liquid two-phase system and a viscous constitutive relation for the solid framework [e.g., *McKenzie*, 1984; *Spiegelman and McKenzie*, 1987].

[29] Up to this point, liquid stress P^l (tension positive) has been used in developing constitutive relations of TH1 and TH2 and in sections 2 and 3 of this paper. However, in the following part of this paper, we use a different sign convention for liquid pressure, denoted $p^L(= -P^l$, compression positive), for consistency with other studies of two-phase dynamics [e.g., *McKenzie*, 1984; *Spiegelman and McKenzie*, 1987]. Governing equations for the conservation of mass and momentum of a solid-liquid two-phase system are generally written as

$$\frac{\partial(\phi\rho^L)}{\partial t} + \nabla \cdot \left(\phi\rho^L \mathbf{v}^L\right) = \Gamma, \tag{13}$$

$$\frac{\partial\{(1-\phi)\rho^S\}}{\partial t} + \nabla \cdot \left\{(1-\phi)\rho^S \mathbf{v}^S\right\} = -\Gamma, \tag{14}$$

$$-\nabla p^L = \frac{\eta_L \phi}{k_\phi}\left(\mathbf{v}^L - \mathbf{v}^S\right) - \rho^L \mathbf{g}, \tag{15}$$

$$p^L_{,i} = \left[\sigma^B_{ij} + p^L\delta_{ij}\right]_{,j} + \bar{\rho}g_i, \tag{16}$$

where $\mathbf{v}^S$ and $\mathbf{v}^L$ are solid and liquid velocities, respectively, ρ^S and ρ^L are solid and liquid densities, respectively, with $\bar{\rho} = (1-\phi)\rho^S + \phi\rho^L$, Γ is the mass exchange rate between solid and liquid, η_L is the liquid viscosity, k_ϕ is the permeability, and $\mathbf{g}$ is the gravitational acceleration. In sections 5 and 6, in order to explore the consequences of grain scale contact anisotropy or melt alignment on the macroscopic dynamics of the two-phase systems, we solve equations (13)–(16) together with equation (9) under two simple boundary conditions. One is a rotary shear deformation under constant torque, which contains a shear stress gradient (section 5). The other is a simple shear deformation under constant shear stress (section 6). The evolution of porosity structure resulting from the anisotropic viscosity given by

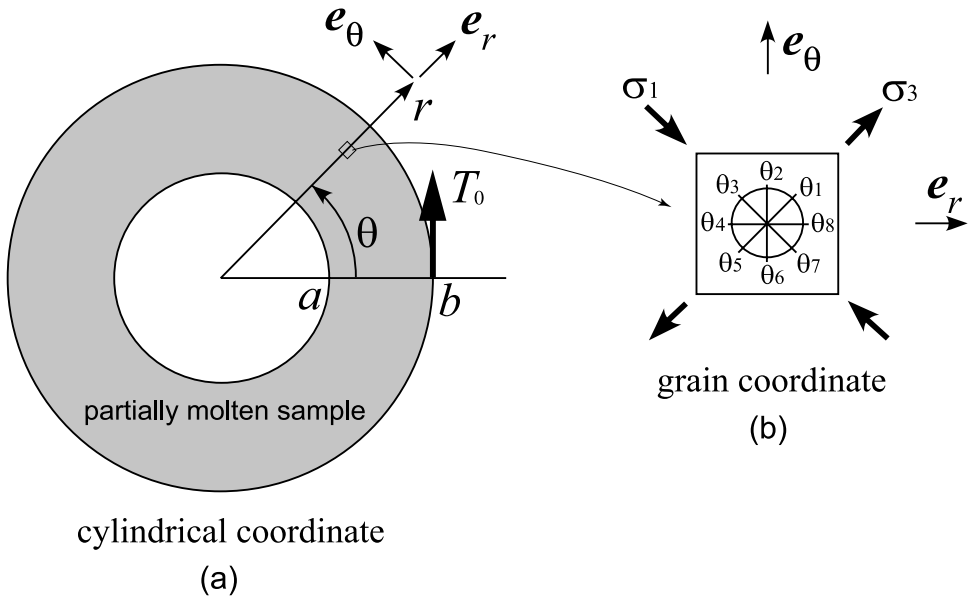

Figure 5. Rotary shear deformation under constant torque T_0. The directions of (a) 2-D cylindrical coordinate system (r, θ) and (b) grain coordinate system θ_k (k = 1–8) are shown. Shear stress $\sigma^B_{r\theta}$ increases with decreasing radius r by r^{-2}.

equation (9) is investigated. This approach implicitly assumes that the timescale for the development of grain-scale melt alignment is much smaller than that for the development of larger-scale porosity structures considered in sections 5 and 6.

5. Melt Migration in Rotary Shear Deformation

[30] The general question explored here is how melt responds to a stress gradient, which can exist in many kinds of fluid dynamical settings, such as cylindrical Couette flow (rotary shear), corner flow, and Poiseuille flow. Stress gradients do not exist in steady state simple shear. Here we focus on the rotary shear problem, for which we can obtain the exact solutions, and demonstrate the occurrence of melt migration up stress gradients. This phenomenon has also been found to occur in rotary shear experiments in partially molten metals [e.g., *Gourlay and Dahle*, 2005]. On the basis of the results of this section, approximate solutions for the ridge and subduction corner flow models are derived in section 7.2.

5.1. Formulation

[31] In rotary shear deformation (Figure 5a), torque is constant at all radii and hence the amplitude of shear stress $\sigma^B_{r\theta}$ increases with decreasing radius r by r^{-2}. We consider a rotary shear deformation of solid-liquid composite system to demonstrate the influence of a shear stress gradient on liquid migration. The cylindrical coordinate system (r, θ) shown in Figure 5a is used. For simplicity, axial symmetry is assumed and hence the derivatives with respect to θ are zero. Stress-induced anisotropy developed under an axially symmetric stress field is also axially symmetric. Hence, as discussed in section 3.2, the 8 contact directions θ_k (k = 1, 2, …, 8) of each grain can be taken as $\theta = \pi k/4$ which are fixed to the cylindrical coordinate system (Figure 5b). By considering the case A contact anisotropy (Figure 2c) and by using liquid pressure p^L (compression positive), the viscous constitutive relation is written as

$$\begin{pmatrix} \sigma^B_{rr}+p^L \\ \sigma^B_{\theta\theta}+p^L \\ \sigma^B_{r\theta} \\ \sigma^B_{\theta r} \end{pmatrix} = \begin{pmatrix} \xi+(\eta+\zeta_1) & \xi-(\eta+\zeta_1) & \zeta_3 & \zeta_3 \\ \xi-(\eta+\zeta_1) & \xi+(\eta+\zeta_1) & \zeta_3 & \zeta_3 \\ \zeta_3 & \zeta_3 & \eta-\zeta_1 & \eta-\zeta_1 \\ \zeta_3 & \zeta_3 & \eta-\zeta_1 & \eta-\zeta_1 \end{pmatrix} \begin{pmatrix} \dot{\varepsilon}^f_{rr} \\ \dot{\varepsilon}^f_{\theta\theta} \\ \dot{\varepsilon}^f_{r\theta} \\ \dot{\varepsilon}^f_{\theta r} \end{pmatrix}, \tag{17}$$

where ξ, η, ζ_1, and ζ_3 are given by equations (6)–(7).

[32] By assuming $\Gamma = 0$, and ρ^S and ρ^L to be constants, and also by neglecting the effects of gravity, governing equations (13)–(16) and (17) are written as

$$\frac{d\phi}{dt} = \frac{1-\phi}{r}\frac{\partial}{\partial r}\left(r v^S_r\right), \tag{18}$$

$$\frac{\partial}{\partial r}\left(r v^S_r\right) = -\frac{\partial}{\partial r}\left(r\phi\left(v^L_r - v^S_r\right)\right), \tag{19}$$

$$-\frac{\partial p^L}{\partial r} = \frac{\eta_L \phi}{k_\phi}\left(v^L_r - v^S_r\right), \tag{20}$$

$$\frac{\partial p^L}{\partial r} = \frac{\partial}{\partial r}\left[\xi\left(\dot{\varepsilon}^f_{rr}+\dot{\varepsilon}^f_{\theta\theta}\right)+2\zeta_3\dot{\varepsilon}^f_{r\theta}\right] + \frac{1}{r^2}\frac{\partial}{\partial r}\left[r^2(\eta+\zeta_1)\left(\dot{\varepsilon}^f_{rr}-\dot{\varepsilon}^f_{\theta\theta}\right)\right], \tag{21}$$

$$0 = \frac{1}{r^2}\frac{\partial}{\partial r}\left[r^2\zeta_3\left(\dot{\varepsilon}^f_{rr}+\dot{\varepsilon}^f_{\theta\theta}\right)+r^2(\eta-\zeta_1)\,2\dot{\varepsilon}^f_{r\theta}\right], \tag{22}$$

where $\dot{\varepsilon}^f_{rr} \pm \dot{\varepsilon}^f_{\theta\theta} = \partial v^S_r/\partial r \pm v^S_r/r$ and $2\dot{\varepsilon}^f_{r\theta} = \partial v^S_\theta/\partial r - v^S_\theta/r$. The boundary conditions are given by

$$\begin{cases} r^2\sigma^B_{r\theta}(r) &= T_0 & \text{for all } r \\ \sigma^B_{rr} &= \sigma_{n0} & \text{at } r = b \\ v^S_\theta &= 0 & \text{at } r = a \\ v^S_r &= v^L_r = 0 & \text{at } r = a, b \end{cases} \tag{23}$$

where a and b represent the inner and outer radii, respectively, and T_0 and σ_{n0} are constants. T_0 represents the torque per unit length in the z direction. Using these equations, we investigate the evolution of the porosity structure with anisotropic viscosity.

5.2. Solution for an Isotropic Case

[33] For comparison, we first solve a simple case that viscosity tensor is isotropic ($\zeta_1 = \zeta_3 = 0$). This corresponds to $\Theta_1/\Theta^0_1 = 1$ in Figure 4. We introduce the nondimensionalized variables defined by

$$\begin{cases} \mathbf{V}^\alpha &= \left(\dfrac{T_0}{2\eta_0 b}\right)^{-1}\mathbf{v}^\alpha \qquad (\alpha = S, L) \\ R &= r/b \\ \tau &= \left(\dfrac{2\eta_0 b^2}{T_0}\right)^{-1} t, \end{cases} \tag{24}$$

where η_0 represents η for the isotropic geometry $\Theta_1/\Theta^0_1 = 1$. The solution for the isotropic case is obtained as

$$\begin{cases} V^S_\theta &= V^L_\theta = R\left(\frac{1}{(a/b)^2} - \frac{1}{R^2}\right) \\ V^S_r &= V^L_r = 0 \\ \frac{d\phi}{d\tau} &= 0. \end{cases} \tag{25}$$

Also, $\sigma^B_{rr} = \sigma^B_{\theta\theta} = -p^L = \sigma_{n0}$ is satisfied in the isotropic case. Therefore, without viscous anisotropy, rotary shear deformation drives neither melt migration nor porosity change.

5.3. Solution for an Anisotropic Case

[34] We demonstrate that with anisotropic viscosity, liquid migrates toward the inner part and hence migrates up stress gradients in the solid framework. Amplitude of the viscous anisotropy generally depends on the shear stress amplitude and porosity ϕ. Here, we consider only the initial evolution of porosity from a constant porosity sample. Hence, ϕ can be approximated to be uniform and constant. The amplitude of $\sigma^B_{r\theta}$ varies with radius. As discussed in section 3.4.1, ξ, η, ζ_1, and ζ_3 are linear functions of the amplitude of $\sigma^B_{r\theta}$ at small $\sigma^B_{r\theta}$ and are constants at large $\sigma^B_{r\theta}$. By assuming that $\sigma^B_{r\theta}$ is large enough for all r (i.e., stress-saturated anisotropy exists throughout the domain), ξ, η, ζ_1, and ζ_3 are treated as constants. Hence, the factor γ, which describes the coupling between shear and isotropic components, defined by equation (11) in section 3, is also constant. If we assume these viscosities and γ to be linear functions of $\sigma^B_{r\theta}$, the mathematical treatment becomes more complicated but the essence of the result does not change. By using the same nondimensional scheme as equations (24), we obtain from equations (19)–(23)

$$\begin{cases} \dfrac{b^2}{\delta_c^2} V^S_r - \dfrac{\partial}{\partial R}\left(\dfrac{\partial V^S_r}{\partial R} + \dfrac{V^S_r}{R}\right) = \dfrac{4\eta_0\gamma}{\xi + \eta + \zeta_1 + \gamma\zeta_3}\dfrac{1}{R^3} \\ V^S_\theta = \dfrac{\eta_0}{\eta - \zeta_1} R\left(\dfrac{1}{(a/b)^2} - \dfrac{1}{R^2}\right) + \gamma R\displaystyle\int_{a/b}^{R} \frac{\nabla\cdot\mathbf{V}^S}{R'} dR'. \end{cases} \tag{26}$$

An important nondimensional parameter in this problem is δ_c/b, representing the ratio between system size and compaction length δ_c, which is defined by

$$\delta_c = \sqrt{\frac{(\xi + \eta + \zeta_1 + \gamma\zeta_3)k_\phi}{\eta_L}}. \tag{27}$$

In the following calculations, we use the values of ξ/η_0, η/η_0, ζ_1/η_0, and ζ_3/η_0 calculated for $\Theta_1/\Theta^0_1 = 0$, which are approximately independent of Θ^0_1 or ϕ, as shown in Figure 4. The inner radius is taken to be $R = 0.5$ (not to be confused with grain radius used by TH1 and TH2).

[35] The solutions for tangential velocity V^S_θ and V^L_θ (Figure 6a), radial velocity V^S_r and V^L_r (Figure 6b), and rate of porosity change $d\phi/d\tau$ versus radius R (Figure 6c) are shown in Figure 6, for $\delta_c/b = 0.5$ (solid lines) and $\delta_c/b = 0.05$ (dotted lines). The first equation of (26) is solved numerically by the finite difference method. In addition to the tangential motion similar to the isotropic case (Figure 6a), outward motion of the solid is balanced by inward motion of the liquid (Figure 6b). Therefore, porosity increases in the inner part and decreases in the outer part (Figure 6c). The result demonstrates that liquid migrates up stress gradients in the solid framework. When the compaction length is much smaller than the system size, the porosity change occurs only in the localized boundary regions (Figure 6c, $\delta_c/b = 0.05$).

5.4. Role of Viscous Anisotropy

[36] We calculate the driving forces for the porosity evolution in rotary shear, to understand why viscous anisotropy causes melt migration up stress gradients. When compaction length (δ_c) is large compared to the system size (b), the dominant driving force for porosity evolution is the same as that for matrix compaction/decompaction, shown in section 5.4.1. When δ_c is smaller than b, the dominant driving force for porosity evolution is the liquid pressure gradient, shown in section 5.4.2. In both cases, coupling between shear and isotropic components, represented by γ, plays a key role.

5.4.1. Effect of Viscous Anisotropy on Matrix Compaction/Decompaction

[37] The driving force for matrix compaction, $-\nabla\cdot\mathbf{v}^S$, is obtained from the constitutive relation (17) as

$$-(\xi + \gamma\zeta_3)\nabla\cdot\mathbf{v}^S = \left(p^B - p^L\right) - \gamma\sigma^B_{r\theta}, \tag{28}$$

where $p^B = -(\sigma^B_{rr} + \sigma^B_{\theta\theta})/2$ represents the bulk or total pressure (compression positive). When viscosity is isotropic ($\gamma = 0$), matrix compaction is driven by effective pressure $p^B - p^L$. However, when viscosity is anisotropic, matrix compaction is driven not only by the isotropic stress component $p^B - p^L$ but also by the shear stress component $\sigma^B_{r\theta}$. For the anisotropy of case A, that is, when weakening occurs in the σ_3 direction, γ is positive at $\sigma^B_{r\theta} > 0$ and negative at $\sigma^B_{r\theta} < 0$ (section 3.3). Hence, $\gamma\sigma^B_{r\theta}$ is always positive, showing that shear stress tends to drive matrix decompaction. Melt migration up stress gradients in the solid occurs because the driving force for decompaction increases with increasing shear stress amplitude (i.e., decreasing r).

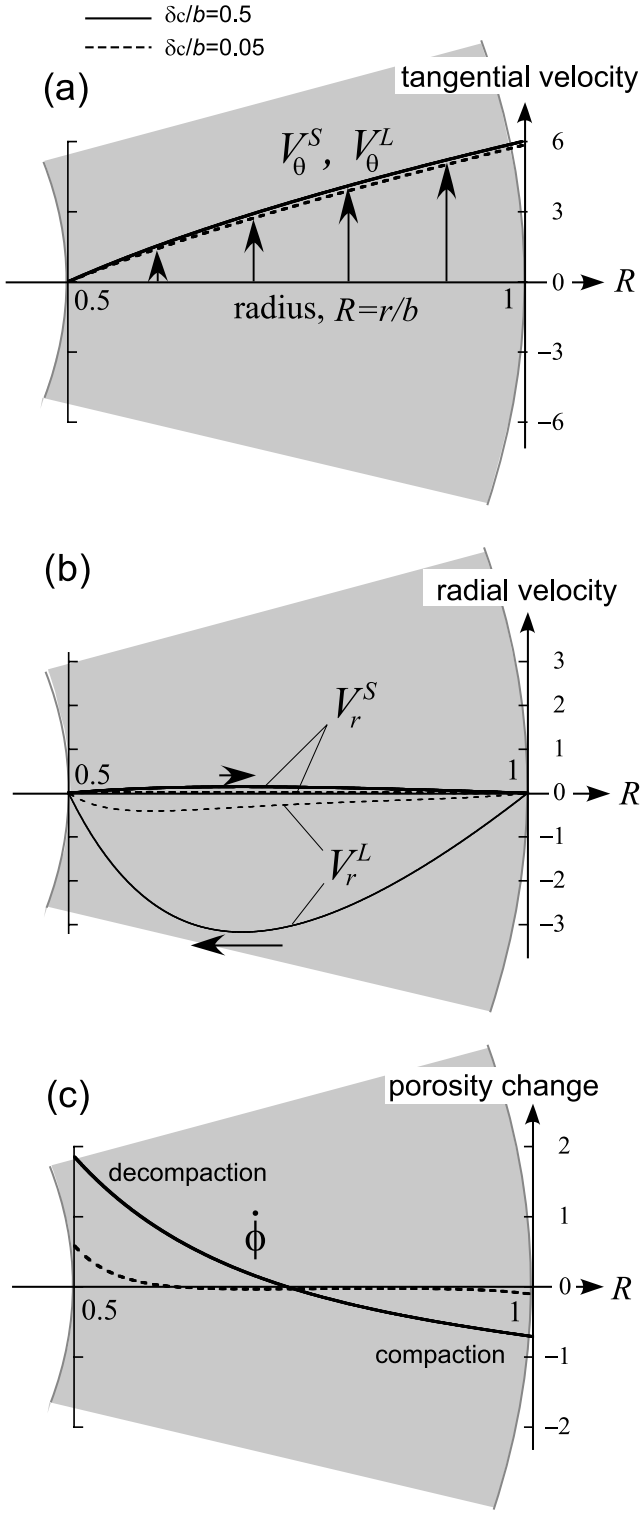

Figure 6. Solutions for the rotary shear deformation of solid-liquid two-phase system with anisotropic viscosity. (a) Tangential velocities of solid (V_θ^S) and liquid (V_θ^L), (b) radial velocities of solid (V_r^S) and liquid (V_r^L), and (c) porosity change versus normalized radius $R = r/b$, for normalized compaction length $\delta_c/b = 0.5$ (solid lines) and $\delta_c/b = 0.05$ (dotted lines). In Figure 6b, V_r^L is shown for $\phi = 0.04$.

[38] For the two cases shown in Figure 6, Figures 7a and 7b show the driving force for matrix compaction, $(p^B - p^L) - \gamma\sigma_{r\theta}^B$, together with liquid pressure p^L, total pressure p^B, and $-\gamma\sigma_{r\theta}^B$. We can see that although effective pressure $p^B - p^L$ is positive for all R, matrix decompaction occurs in the inner part because of the significant tendency for decompaction produced by $\gamma\sigma_{r\theta}^B$. When compaction length

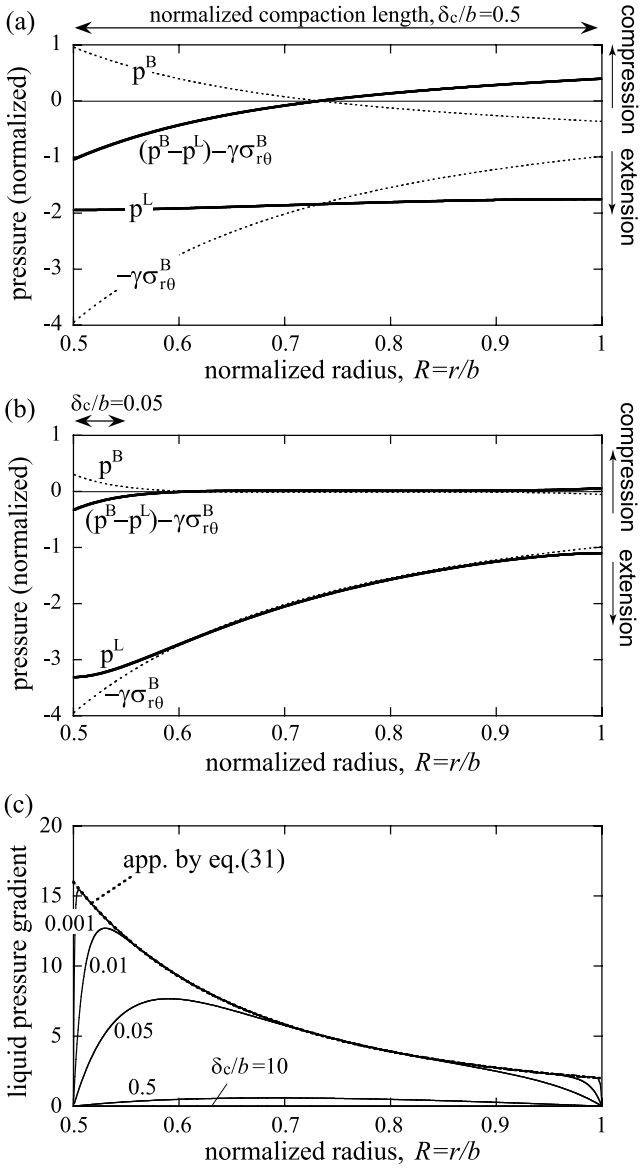

Figure 7. Solutions for the rotary shear deformation of solid-liquid two-phase system with anisotropic viscosity. (a, b) Stress states of the system with normalized compaction length $\delta_c/b = 0.5$ (Figure 7a) and $\delta_c/b = 0.05$ (Figure 7b). $(p^B - p^L) - \gamma\sigma_{r\theta}^B$ represents the driving force for matrix compaction, where p^B and p^L represent the total and liquid pressures (compression positive), respectively, and $-\gamma\sigma_{r\theta}^B$ represents a contribution from shear stress due to the coupling between shear and isotropic components. (c) Liquid pressure gradients for various δ_c/b along with an approximation by equation (31). Pressures normalized to $\sigma_{r\theta}^B|_{r=b}$ are plotted under $\sigma_{n0} = 0$.

δ_c is large compared to system size b, the driving force for the matrix compaction/decompaction is large and heterogeneous, whereas the liquid pressure gradient is nearly zero (Figures 7a and 7c). However, when δ_c is much smaller than b, the driving force for the matrix compaction/decompaction is nearly zero except for the localized regions, whereas large liquid pressure gradient develops in the direction of liquid migration (Figures 7b and 7c).

5.4.2. Effect of Viscous Anisotropy on Liquid Pressure Gradient

[39] By substituting equation (2) into equation (16) with $p^L = -P^f$, we obtain

$$p^L_{,i} = \frac{1}{2}\left[C^B_{ijkl}\left(v^S_{k,l} + v^S_{l,k}\right)\right]_{,j} + \bar{\rho} g_i. \tag{29}$$

Equation (29) describes the effects of matrix deformation $\mathbf{v}^S$ on the liquid pressure gradient, which drives liquid flow by equation (15). When C^B_{ijkl} is isotropic, the first term in the right-hand side of equation (29) consists of $(\xi + \eta/3)\nabla(\nabla \cdot \mathbf{v}^S)$ and $\eta\nabla^2\mathbf{v}^S$. Hence, for volume conserving shear deformation of the matrix ($\nabla \cdot \mathbf{v}^S = 0$), only deformation with nonzero $\nabla^2\mathbf{v}^S$ can produce a liquid pressure gradient [*Spiegelman and McKenzie*, 1987; *Phipps Morgan*, 1987]. When C^B_{ijkl} is anisotropic, however, there is a range of mechanisms by which the matrix shear deformation can create a liquid pressure gradient. For simplicity, we consider a simple shear dominantly given by $v^S_{x,y}$ and varying in the y direction due to stress gradient (e.g., Figure 2a). For case A contact anisotropy, that is, when weakening occurs in the σ_3 direction, the off-diagonal components C^B_{yyxy} and $C^B_{yyyx}(= \zeta_3)$ are nonzero and have the opposite sign of $v^S_{x,y}$ (section 3.3). Therefore, the y component of the liquid pressure gradient given by equation (29), $p^L_{,y} = [C^B_{yyxy}v^S_{x,y}]_{,y}$, predicts migration up the solid stress gradient. For the solid flow field illustrated in Figure 2a ($v^S_{x,y} > 0$, $\zeta_3 < 0$, and $v^S_{x,yy} < 0$), equation (29) predicts $p^L_{,y} = \zeta_3 v^S_{x,yy} > 0$ and hence predicts a flow toward the $-y$ direction.

[40] *Spiegelman and McKenzie* [1987] proposed a simple method to estimate liquid pressure gradients by substituting into equation (29) an approximate solution of matrix deformation $\mathbf{v}^S$ obtained under the assumption of constant porosity. Here, we assess the applicability of this method to systems with anisotropic viscosity, by comparing the liquid pressure gradients estimated from the simple method to the exact solutions for the rotary shear systems. In section 7.2, we further apply this simple model to estimate the effect of viscous anisotropy on melt streamlines in the mantle at ridges and subduction zones.

[41] To solve the rotary shear model under the assumption of constant porosity, equation (17) is first modified to a form of viscosity for an incompressible fluid, a general form of which is presented in Appendix A. Then, equation (17) becomes

$$\begin{pmatrix} \sigma^B_{rr} + p^B \\ \sigma^B_{\theta\theta} + p^B \\ \sigma^B_{r\theta} \\ \sigma^B_{\theta r} \end{pmatrix} = \begin{pmatrix} 2(\eta+\zeta_1) & 0 & 0 & 0 \\ 0 & 2(\eta+\zeta_1) & 0 & 0 \\ 0 & 0 & \eta-\zeta_1 & \eta-\zeta_1 \\ 0 & 0 & \eta-\zeta_1 & \eta-\zeta_1 \end{pmatrix} \cdot \begin{pmatrix} \dot{\varepsilon}^f_{rr} \\ \dot{\varepsilon}^f_{\theta\theta} \\ \dot{\varepsilon}^f_{r\theta} \\ \dot{\varepsilon}^f_{\theta r} \end{pmatrix}. \tag{30}$$

Under equation (30), matrix deformation of the rotary shear system is solved as $\dot{\varepsilon}^f_{r\theta} = \dot{\varepsilon}^f_{\theta r} = T_0/\{2r^2(\eta - \zeta_1)\}$, $\dot{\varepsilon}^f_{rr} = 0$, and $\dot{\varepsilon}^f_{\theta\theta} = 0$. By substituting this solution into equation (21), we obtain

$$\frac{\partial p^L}{\partial r} = \frac{2\gamma T_0}{r^3}. \tag{31}$$

The liquid pressure gradient given by equation (31) is shown in Figure 7c (thick dotted line), along with the exact solutions of equations (17)–(23) for various values of δ_c/b (solid lines). The solutions for small δ_c/b, where compaction/decompaction is significant only near the inner and outer radii, are closely approximated by equation (31). As δ_c/b increases, the liquid pressure gradient deviates from equation (31), because effects of matrix compaction/decompaction become nonnegligible. Therefore, for the case of $\delta_c/b \ll 1$, the liquid pressure gradient can be closely approximated by the simple model.

[42] In section 7.2, the simple method tested here for the rotary shear system is applied to the mantle flow at ridges and subduction zones, by assuming that the compaction length is much smaller than the spatial scale of the system. Use of equation (17) in the rotary shear model is based on the assumption that the σ_3 direction is 45° to the shear plane, which is the case with isotropic viscosity. With anisotropic viscosity, the deviatoric component $\dot{\varepsilon}^f_{rr} - \dot{\varepsilon}^f_{\theta\theta}$ is not exactly zero and affects the principal stress directions. However, using the exact solutions of the rotary shear system, we verified that this effect is insignificant especially when the spatial scale is much larger than the compaction length; the deviation of the σ_3 direction from 45° reaches a maximum at the boundary ($r = a$, b) but still <6° for $\delta_c/b > 1$, <2° for $\delta_c/b < 0.1$ and <1° for $\delta_c/b < 0.05$. Therefore, in section 7.2, we estimate magnitude and orientation of grain-scale anisotropy from the stress with isotropic viscosity.

6. Linear Analysis of the Formation of Melt-Rich Bands by Simple Shear

[43] *Holtzman et al.* [2003a, 2003b] deformed partially molten rocks under simple shear and observed the formation of melt-rich bands, which develop at small strains (<1) and persist at low angles (∼15–20°) to the plane of shear. Unstable growth of melt-rich bands in porous media undergoing pure shear was predicted in a model developed by *Stevenson* [1989] with porosity weakening viscosity. *Spiegelman* [2003] extended this model to simple shear and showed that the observed low angle cannot be explained by the simple porosity weakening model because the maximum growth rate occurs at higher angle (∼45°). *Katz et al.* [2006] showed that the experimentally observed low angle can be explained by considering a model with porosity-weakening and non-Newtonian viscosity, because the maximum growth rate occurs at low angles due to a balance of porosity weakening and strain rate weakening. Here, we consider this problem on the basis of our new model with porosity-weakening and anisotropic viscosity and show that the observed low angle can be explained by viscous anisotropy, without taking into account a non-Newtonian viscosity.

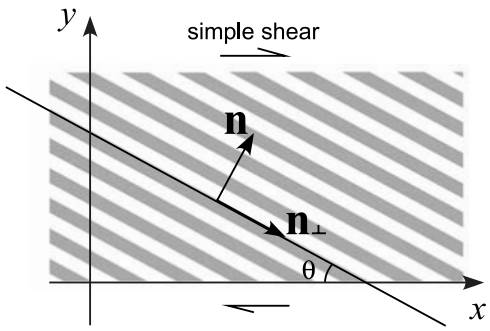

Figure 8. For linear analysis, a plane wave perturbation in melt fraction which makes angle θ with the shear plane is considered. The unit vectors $\mathbf{n}$ and $\mathbf{n}_\perp$ are normal to the perturbation plane and perpendicular to $\mathbf{n}$ (parallel to the perturbation plane), respectively.

6.1. Formulation

[44] The analysis follows closely the linear stability analysis developed by *Spiegelman* [2003] and *Katz et al.* [2006]. The present analysis is based on the viscosity tensor given by equation (9), including cases A–C (Figures 2c–2e). Liquid pressure $p^L(=-P^l)$ is used in this section. By assuming $\Gamma = 0$, and ρ^L and ρ^S be constants, and also by neglecting the effects of gravity, governing equations (13)–(16) are written as

$$\frac{d\phi}{dt} = (1-\phi)\,\nabla\cdot\mathbf{v}^S, \tag{32}$$

$$\nabla\cdot\mathbf{v}^S = -\nabla\cdot\left(\phi(\mathbf{v}^L-\mathbf{v}^S)\right), \tag{33}$$

$$-\nabla p^L = \frac{\eta_L\phi}{k_\phi}\left(\mathbf{v}^L-\mathbf{v}^S\right), \tag{34}$$

$$\frac{\partial p^L}{\partial x} = \frac{\partial}{\partial x}\Big[(\xi+\eta+\zeta_1+2\zeta_2)\,\dot{\varepsilon}^f_{xx} + (\xi-\eta-\zeta_1)\,\dot{\varepsilon}^f_{yy} + 2\zeta_3\dot{\varepsilon}^f_{xy}\Big] + \frac{\partial}{\partial y}\Big[\zeta_3\left(\dot{\varepsilon}^f_{xx}+\dot{\varepsilon}^f_{yy}\right) + 2(\eta-\zeta_1)\,\dot{\varepsilon}^f_{xy}\Big], \tag{35}$$

$$\frac{\partial p^L}{\partial y} = \frac{\partial}{\partial y}\Big[(\xi-\eta-\zeta_1)\,\dot{\varepsilon}^f_{xx} + (\xi+\eta+\zeta_1-2\zeta_2)\,\dot{\varepsilon}^f_{yy} + 2\zeta_3\dot{\varepsilon}^f_{xy}\Big] + \frac{\partial}{\partial x}\Big[\zeta_3\left(\dot{\varepsilon}^f_{xx}+\dot{\varepsilon}^f_{yy}\right) + 2(\eta-\zeta_1)\,\dot{\varepsilon}^f_{yx}\Big]. \tag{36}$$

Following the previous studies, we consider the case of infinite domains.

6.1.1. Stationary State

[45] First, we consider an infinite system with homogeneous melt fraction $\phi = \phi^0$, which has a homogeneous and anisotropic viscosity tensor described by ξ^0, η^0, ζ_1^0, ζ_2^0, and ζ_3^0. The coupling factor defined by equation (11) is written as $\gamma^0 = -\zeta_3^0/(\eta^0-\zeta_1^0)$. As a stationary state solution satisfying equations (32)–(36), we consider a uniform simple shear deformation in the x direction under constant shear and normal stresses, σ_{xy}^{B0}, σ_{xx}^{B0}, and $\sigma_{yy}^{B0}(=\sigma_{xx}^{B0})$,

$$\begin{cases} 2\dot{\varepsilon}^{f0}_{xy} = \sigma^{B0}_{xy}/(\eta^0-\zeta_1^0) \\ v_x^{S0} = v_x^{L0} = 2\dot{\varepsilon}^{f0}_{xy}\cdot y \\ v_y^{S0} = v_y^{L0} = 0 \\ -p^{L0} = \sigma^{B0}_{yy} + \gamma^0\sigma^{B0}_{xy}. \end{cases} \tag{37}$$

6.1.2. Linear Stability Analysis

[46] We investigate the stability of the stationary state against a plane wave perturbation in melt fraction ϕ (Figure 8). We define nondimensionalized variables using the stationary state solution, as

$$\begin{cases} \tau = 2\dot{\varepsilon}^{f0}_{xy}\,t \\ \mathbf{X} = \mathbf{x}/\delta_c^0 \\ \mathbf{V}^\alpha = \mathbf{v}^\alpha/(2\dot{\varepsilon}^{f0}_{xy}\,\delta_c^0) \quad (\alpha = S,L) \\ P^L = p^L/\sigma^{B0}_{xy}, \end{cases} \tag{38}$$

where nondimensional time τ represents the total simple shear, and δ_c^0 represents the compaction length for $\phi=\phi^0$. In this section, δ_c is defined by

$$\delta_c = \sqrt{\frac{(\xi+\eta-3\zeta_1)k_\phi}{\eta_L}}, \tag{39}$$

which is slightly different from (27).

[47] A small perturbation in ϕ and small perturbations in the relevant properties are written as

$$\begin{cases} \phi(\mathbf{X},\tau) = \phi^0 + \epsilon\,\phi^1(\mathbf{X},\tau) \\ \xi(\phi) = \xi^0(\phi^0) + \epsilon\,\xi^1(\phi^1) \\ \eta(\phi) = \eta^0(\phi^0) + \epsilon\,\eta^1(\phi^1) \\ \zeta_i(\phi) = \zeta_i^0(\phi^0) + \epsilon\,\zeta_i^1(\phi^1) \qquad (i=1,2,3) \\ V_x^\alpha(\mathbf{X},\tau) = V_x^{\alpha\,0}(Y) + \epsilon\,V_x^{\alpha\,1}(\mathbf{X},\tau) \quad (\alpha=S,L) \\ V_y^\alpha(\mathbf{X},\tau) = \epsilon\,V_y^{\alpha\,1}(\mathbf{X},\tau) \qquad (\alpha=S,L) \\ P^L(\mathbf{X},\tau) = P^{L0} + \epsilon\,P^{L1}(\mathbf{X},\tau), \end{cases} \tag{40}$$

where $\epsilon \ll 1$. In the following analysis, the melt fraction dependences of $\eta^1-\zeta_1^1$ and ζ_3^1 play important roles. Using the two factors $\lambda_\eta(>0)$ and $\lambda_\zeta(>0)$ introduced in section 3.4.2, these dependences are written in linearized forms as

$$\begin{cases} -\dfrac{\eta^1-\zeta_1^1}{\eta^0-\zeta_1^0} = \lambda_\eta\phi^1 \\ -\dfrac{\zeta_3^1}{\zeta_3^0} = \lambda_\zeta\phi^1. \end{cases} \tag{41}$$

As discussed in section 3.4.2, we assume that $\lambda_\eta \simeq \lambda_\zeta \simeq \lambda$, where λ is an experimentally obtained porosity weakening factor which has a value of $\sim$25.

[48] Following the previous studies [*Spiegelman*, 2003; *Katz et al.*, 2006], we seek solutions for the full linearized equations of the form

$$\begin{cases} \phi^1(\mathbf{X},\tau) = e^{s(\tau)} e^{i\mathbf{K}\cdot\mathbf{X}} \\ \mathbf{V}^{L1}(\mathbf{X},\tau) = A^L(\tau)\,\phi^1(\mathbf{X},\tau)\,\mathbf{n} + B^L(\tau)\,\phi^1(\mathbf{X},\tau)\,\mathbf{n}_\perp \\ \mathbf{V}^{S1}(\mathbf{X},\tau) = A^S(\tau)\,\phi^1(\mathbf{X},\tau)\,\mathbf{n} + B^S(\tau)\,\phi^1(\mathbf{X},\tau)\,\mathbf{n}_\perp \\ P^{L1}(\mathbf{X},\tau) = A^P(\tau)\,\phi^1(\mathbf{X},\tau), \end{cases} \tag{42}$$

where nondimensional wave number $\mathbf{K}$, unit vector $\mathbf{n}$ normal to the plane of perturbation, and unit vector $\mathbf{n}_\perp$ perpendicular to $\mathbf{n}$ or parallel to the perturbation plane are given by

$$\begin{cases} \mathbf{K} = \begin{pmatrix} K_x \\ K_y \end{pmatrix} = \begin{pmatrix} K_x^0 \\ K_y^0 - K_x^0\tau \end{pmatrix} \\ \mathbf{n} = \dfrac{\mathbf{K}}{K} = \begin{pmatrix} \sin\theta(\tau) \\ \cos\theta(\tau) \end{pmatrix} \\ \mathbf{n}_\perp = \begin{pmatrix} \cos\theta(\tau) \\ -\sin\theta(\tau) \end{pmatrix} \end{cases} \tag{43}$$

with $\mathbf{K}^0 = \mathbf{K}(\tau = 0)$ and $K = |\mathbf{K}|$. θ represents the angle which the plane wave perturbation makes with the shear plane (Figure 8). From equations (33) and (34), we obtain

$$\begin{cases} A^P = h_0 \dfrac{A^S}{iK} \\ A^L = -\dfrac{1-\phi^0}{\phi^0} A^S \\ B^L = B^S, \end{cases} \tag{44}$$

where

$$h_0 = \frac{\xi^0 + \eta^0 - 3\zeta_1^0}{\eta^0 - \zeta_1^0}. \tag{45}$$

In the previous studies, solid velocity was decomposed into its compressible and incompressible components using potentials U_1 and ψ_1^s, respectively [*Spiegelman*, 2003; *Katz et al.*, 2006]. The parameters A^S and B^S defined by equation (42) can be related to U_1 and ψ_1^s as $iKA^S\phi^1 = \nabla^2 U_1$ and $iKB^S\phi^1 = \nabla^2\psi_1^s$. We introduce here matrix decompaction C and rotation Ω defined by

$$\begin{cases} C = iKA^S \\ \Omega = iKB^S, \end{cases} \tag{46}$$

which can be identified with C^* and $(ik)^2\psi^*$, respectively, used by *Spiegelman* [2003] and *Katz et al.* [2006]. From equations (35) and (36), C and Ω are solved as

$$\begin{pmatrix} \dfrac{h_0}{K^2} + h_0 + \Delta_{11} & \Delta_{12} \\ \Delta_{21} & 1 + \Delta_{22} \end{pmatrix} \begin{pmatrix} C \\ \Omega \end{pmatrix} = \begin{pmatrix} 2\lambda_\eta n_x n_y - \lambda_\zeta \gamma^0 \\ \lambda_\eta (n_y^2 - n_x^2) \end{pmatrix}, \tag{47}$$

where

$$\begin{cases} \Delta_{11} = 2h_1 n_x^4 + 2h_2 n_y^4 - 4\gamma^0 n_x n_y \\ \Delta_{12} = \Delta_{21} = 2h_1 n_x^3 n_y - 2h_2 n_x n_y^3 + \gamma^0(n_x^2 - n_y^2) \\ \Delta_{22} = 2n_x^2 n_y^2 (h_1 + h_2) \end{cases} \tag{48}$$

and

$$\begin{cases} h_1 = \dfrac{2\zeta_1^0 + \zeta_2^0}{\eta^0 - \zeta_1^0} \\ h_2 = \dfrac{2\zeta_1^0 - \zeta_2^0}{\eta^0 - \zeta_1^0}. \end{cases} \tag{49}$$

From equation (32), we obtain the growth rate as

$$\begin{aligned} \frac{ds}{d\tau} &= (1-\phi^0)C \\ &= (1-\phi^0)\cdot \frac{(1+\Delta_{22})(2\lambda_\eta n_x n_y - \lambda_\zeta\gamma^0) - \Delta_{12}\lambda_\eta(n_y^2 - n_x^2)}{(1+\Delta_{22})(h_0/K^2 + h_0 + \Delta_{11}) - \Delta_{12}\Delta_{21}}. \end{aligned} \tag{50}$$

When viscosity is isotropic, Δ_{ij} (i, j = 1, 2), γ^0, and ζ_{1-3}^0 vanish, and equation (50) becomes

$$\frac{ds}{d\tau} = (1-\phi^0)\left(\frac{\eta^0}{\xi^0 + \eta^0}\right)\frac{2\lambda_\eta n_x n_y}{K^{-2} + 1}, \tag{51}$$

which is equal to the result of *Spiegelman* [2003, equation (27)]. (The factor $\xi = \eta_0/(\zeta_0 + 4\eta_0/3)$ of *Spiegelman* [2003] with bulk and shear viscosities ζ_0 and η_0, and the factor $\eta^0/(\xi^0 + \eta^0)$ in equation (51) with bulk and shear viscosities ξ^0 and η^0 are different by the factor 4/3 in the denominator, because this present study is based on the constitutive relation derived in two dimensions.)

[49] The exponential factor s of the amplitude of the wave which makes angle θ with the shear plane at nondimensional time (or strain) τ is given by

$$s(\theta,\tau) = \int_{\tau'=0}^{\tau'=\tau} \left.\frac{ds}{d\tau}\right|_{\theta(\tau')} d\tau', \tag{52}$$

where θ (τ') at $\tau' \le \tau$ is calculated from equations (43) with initial angle θ_0 given by

$$\theta_0 = \arctan\left(\frac{\sin\theta(\tau)}{\cos\theta(\tau) + \tau\cdot\sin\theta(\tau)}\right). \tag{53}$$

6.2. Growth Rate of Melt-Rich Bands

[50] When the nondimensional wave number K is much larger than 1 (perturbation wavelength is much smaller than the compaction length δ_c^0), the growth rate given by equation (50) is almost independent of K, and when K becomes smaller than 1 (perturbation wavelength is larger than δ_c^0), it decreases with decreasing K. Therefore, we only consider further the former condition and assume that the growth rate

is independent of K. Figure 9a shows growth rate versus θ at nondimensional time (or strain) $\tau = 0$ predicted from our model at $K \gg 1$. The calculation is performed for the anisotropic contact geometry of case A (Figure 2c). The curve of $\Theta_1/\Theta_1^0 = 1$ shows the isotropic case, and the curves of $\Theta_1/\Theta_1^0 < 1$ show the anisotropic cases. For the isotropic case, the growth rate is positive at $\theta < 90°$ and negative at $\theta > 90°$, with a peak value at $\theta = 45°$, consistent with the work by *Spiegelman* [2003]. As anisotropy increases, the growth rate at $\theta = 45°$ decreases and the curve labeled $\Theta_1/\Theta_1^0 = 1/3$ shows two peaks at $\theta \simeq 15°$ and $\theta \simeq 75°$.

[51] The effect of increasing strain is shown in terms of the logarithmic amplitude $s(\theta, \tau)$ versus θ at $\tau = 1$, in Figure 9b. For the anisotropic case with $\Theta_1/\Theta_1^0 = 1/3$, the peak initially at $\theta \simeq 15°$ stays at almost the same direction, whereas the peak initially at $\theta \simeq 75°$ moves to about 90° and the amplitude of the high-angle peak is smaller than that of the lower angle peak. The different behavior of the two peaks is explained by the rotation of the plane wave perturbation caused by the background simple shear [*Spiegelman.*, 2003]. Because the rotation is slower for lower angle, the plane wave perturbations initially near the low-angle peak grow more efficiently than those initially near the high-angle peak, which rotate quickly toward higher angle and begin to shrink at $\theta > 90°$.

[52] To illustrate how the system evolves, we show amplitude $e^{s(\theta,\tau)}$ versus θ with increasing τ in Figure 9c, for the anisotropic case with $\Theta_1/\Theta_1^0 = 1/3$ and for $(1 - \phi^0)\lambda_\eta = 25$. A sharp peak develops at small strain ($\tau < 1$) and persists at low angle ($\sim 15-25°$) for $\tau \leq 4$. A solid circle on each line plots the angle and amplitude of the perturbation initially at $\theta = 15°$, showing that the apparent rotation of melt-rich bands is much slower than the rotation of the matrix, especially at $\tau > 1$. This separation indicates that the dominant bands are not fixed to the solid matrix, implying that melt must migrate relative to the solid matrix. Squares mark experimental data at the position of $(\theta, \tau + 1)$, such that the short horizontal distances between symbols and peaks indicate the good agreement between measured and predicted angles.

6.3. Role of Viscous Anisotropy

[53] For understanding the effect of viscous anisotropy on the formation of melt-rich bands, equation (47) is further written as

$$\begin{pmatrix} \frac{h_0}{K^2} + h_0 + \Delta_{11} & \Delta_{12} \\ \Delta_{21} & 1 + \Delta_{22} \end{pmatrix} \begin{pmatrix} C \\ \Omega \end{pmatrix} = \lambda \begin{pmatrix} \sigma_n^0 + P^{L0} \\ \sigma_t^0 \end{pmatrix}, \quad (54)$$

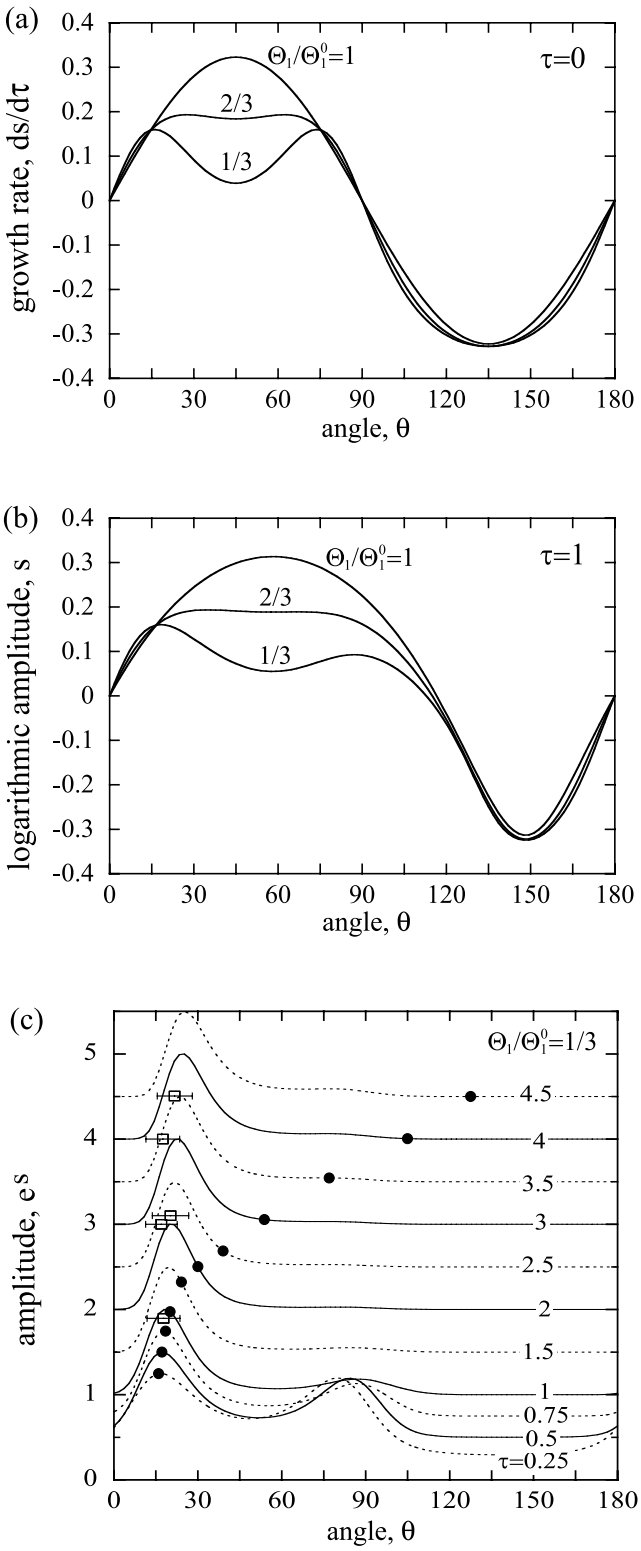

Figure 9. (a) Growth rate $ds/d\tau$ of melt-rich band versus θ at nondimensional time (or strain) $\tau = 0$ for isotropic viscosity ($\Theta_1/\Theta_1^0 = 1$) and for anisotropic viscosity of case A ($\Theta_1/\Theta_1^0 = 2/3, 1/3$). Value of $ds/d\tau$ divided by $\lambda(1 - \phi^0)$ is shown. (b) Logarithmic amplitude s versus θ at $\tau = 1$ for isotropic viscosity ($\Theta_1/\Theta_1^0 = 1$) and for anisotropic viscosity of case A ($\Theta_1/\Theta_1^0 = 2/3, 1/3$). Value of s divided by $\lambda(1 - \phi^0)$ is shown. (c) Amplitude e^s versus θ at various τ for anisotropic viscosity of case A with $\Theta_1/\Theta_1^0 = 1/3$. Amplitude normalized to the maximum value at each τ, $e^s/e^{s(\max)}$, is plotted at the position of $(\theta, \tau + e^s/e^{s(\max)})$. Solid circles show the evolution in angle and amplitude of the perturbation initially at $\theta = 15°$. Squares show experimental data at the position of $(\theta, \tau + 1)$.

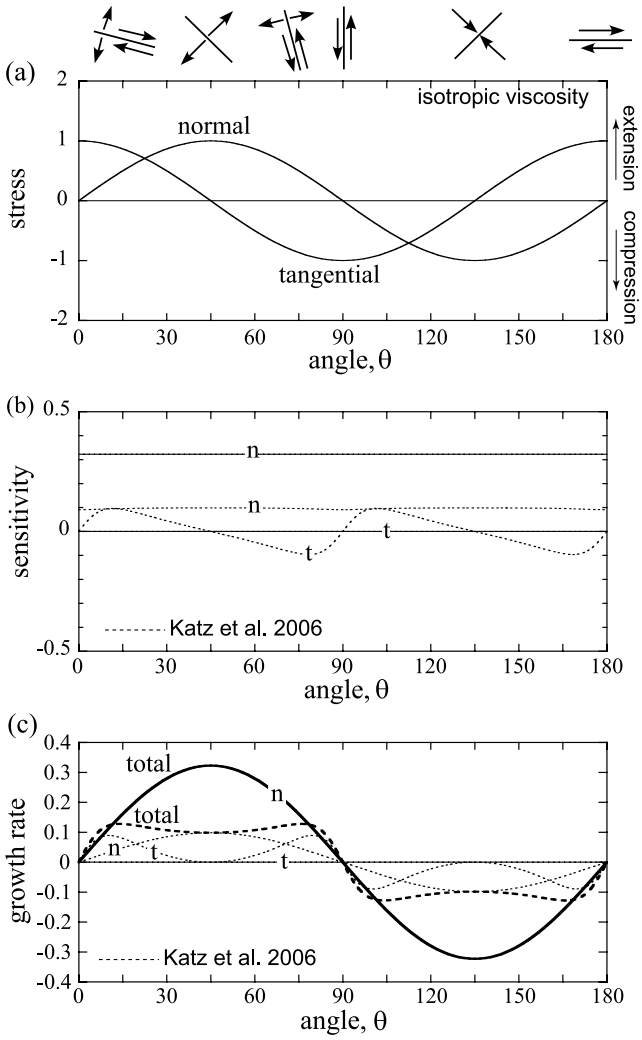

Figure 10. Mechanism for the unstable growth of melt-rich band with isotropic viscosity. (a) Components of the effective stress normal and tangential to the plane of perturbation which makes angle θ with the shear plane (tension positive). (b) Sensitivities of matrix decompaction C to normal (labeled n) and tangential (labeled t) stresses. (c) Growth rate $ds/d\tau$ of melt-rich band produced by normal stress (labeled n) and tangential stress (labeled t) and the total of these two (thick line). Solid and dotted lines in Figures 10b and 10c show the linear viscosity model [*Spiegelman*, 2003] and the nonlinear viscosity model [*Katz et al.*, 2006], respectively.

where σ_n^0 and σ_t^0 represent the stresses normal and tangential, respectively, to the plane of perturbation. These stresses are given by

$$\begin{cases} \sigma_n^0 + P^{L0} = \sigma_{ij}^{B0} n_i n_j / \sigma_{xy}^{B0} + P^{L0} = 2 n_x n_y - \gamma^0 \\ \sigma_t^0 \qquad\quad = \sigma_{ij}^{B0} n_i (n_\perp)_j / \sigma_{xy}^{B0} \qquad = n_y^2 - n_x^2, \end{cases} \tag{55}$$

and $\lambda_\eta = \lambda_\zeta = \lambda$ is assumed. As the first line of equation (50) shows, a positive value of matrix decompaction C indicates the unstable growth of melt-rich bands. Hence, the right-hand side and left-hand side of equation (54) represent the driving force and the resistance, respectively, for the band growth; when $K \gg 1$ the resistance to band growth is dominated by the matrix deformation. When viscosity is isotropic, $\Delta_{ij} = 0$ ($i, j = 1, 2$) and left-hand side of equation (54) becomes a diagonal matrix. In this case, C is produced only by the effective normal stress $\sigma_n^0 + P^{L0}$ and is not affected by the tangential stress σ_t^0. When viscosity is anisotropic, the off-diagonal components Δ_{12} and Δ_{21} are nonzero and C is produced not only by the normal stress but also by the tangential stress.

[54] The detailed mechanisms of band formation with isotropic and anisotropic viscosities predicted by equation (54) are illustrated by showing the driving forces $\sigma_n^0 + P^{L0}$ and σ_t^0 (Figures 10a and 11a), sensitivity of C to these forces (Figures 10b and 11b), and the growth rates produced by

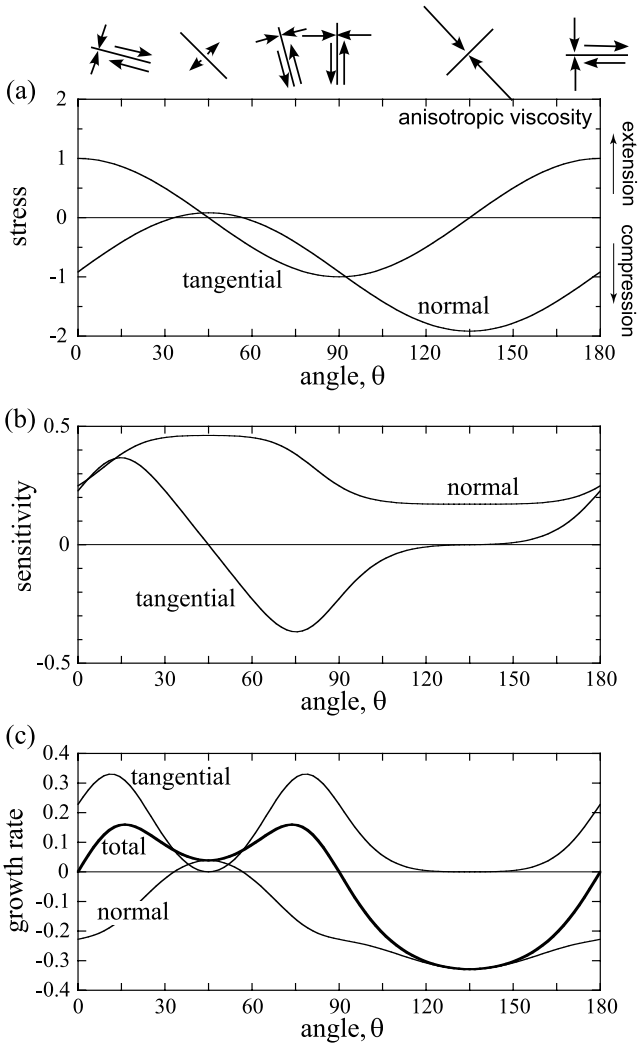

Figure 11. Mechanism for the unstable growth of melt-rich band with case A anisotropic viscosity with $\Theta_1/\Theta_1^0 = 1/3$. (a) Components of the effective stress normal and tangential to the plane of perturbation which makes angle θ with the shear plane (tension positive). (b) Sensitivities of matrix decompaction C to normal and tangential stresses. (c) Growth rate $ds/d\tau$ of melt-rich band produced by normal stress and tangential stress and the total of these two (thick line).

the two driving forces (Figures 10c and 11c). Sensitivity to the effective normal stress is given by $(1 + \Delta_{22})/det$ and the sensitivity to the tangential stress is given by $-\Delta_{12}/det$, where $det = (h_0 + \Delta_{11})(1 + \Delta_{22}) - \Delta_{12}\Delta_{21}$. For isotropic viscosity, the sensitivity to the tangential stress is zero for all θ (solid line labeled "t" in Figure 10b), and a positive value of the growth rate results only from an extensional effective normal stress ($\sigma_n^0 + P^{L0} > 0$). For the anisotropic case, the effective normal stress is more compressive than the isotropic case due to the effect of γ^0 (equation (55) and Figure 11a), which leads to the reduction of the growth rate driven by the effective normal stress (Figure 11c). The significant decrease of the growth rate at $\theta = 45°$ in the anisotropic case (Figure 9a) is due to this reduction of the extensional effective normal stress. Although the growth rate produced by the effective normal stress is mostly negative, the growth rate produced by the tangential stress is positive and has two peaks at low and high angles (Figure 11c). We therefore conclude that with isotropic viscosity, the melt rich bands are dominantly produced by the effective normal stress, whereas with the anisotropic viscosity, the melt-rich bands are dominantly produced by the tangential stress. The change in peak angle due to the viscous anisotropy (Figure 9a) reflects such difference.

6.4. Comparison to the Model of *Katz et al.* [2006]

[55] Another mechanism in which tangential stress affects the band formation and causes a change in the direction of maximum growth rate was proposed by *Katz et al.* [2006]. The band formation mechanism in their model can also be described in the same form as equation (54) (Appendix B) and is shown in Figure 10 by the dotted lines. Although their model assumes isotropic viscosity, the sensitivity of C to the tangential stress is nonzero due to the strain rate-weakening effect caused by the power law creep (dotted line labeled "t" in Figure 10b). The growth rate produced by the tangential stress has two peaks at low and high angles (dotted line labeled "t" in Figure 10c).

[56] The amplitude $e^{s(\theta,\tau)}$ versus θ predicted from the model of *Katz et al.* [2006] is shown in Figure B1 in Appendix B with the result of this study for comparison. As shown in Appendix B, the values of the parameters used by *Katz et al* [2006] ($\alpha = -25$ and $n = 6$) overestimate the porosity-weakening effect. We therefore show the results of their model both for the parameter values similar to their original values ($((1 - \phi^0)\lambda/n = 25$, $n = 6$, and $\xi^0/\eta^0 = 10$; solid lines in Figure B1) and for the modified values ($((1 - \phi^0)\lambda/n = 25/6$, $n = 6$, and $\xi^0/\eta^0 = 10$; dotted lines in Figure B1). When the modified values are used, the rapid formation of low-angle melt-rich bands ($\tau \leq 1$) is better explained by the present model than the model of *Katz et al.* [2006].

[57] *Katz et al.* [2006] performed not only the linear stability analysis but also a fully nonlinear simulation, which becomes important especially at large τ. A good agreement between the linear stability analysis and the simulation was obtained by *Katz et al.* [2006] for the stability of the band angle. A similar fully nonlinear analysis with anisotropic viscosity is necessary to further explore the mechanisms for band stability proposed here.

6.5. Comparison to the Experimental Results

[58] These results are consistent with several basic observations in experiments: first, the melt alignment and orientation at the grain scale that cause the anisotropic viscosity must precede the segregation at wavelengths longer than the grain scale. This sequence is observed in experiments, with melt pockets aligning at the grain scale before shear strains of 1, followed by longer wavelength segregation [*Holtzman and Kohlstedt*, 2007]. Second, the low-angle bands are more stable than higher angle bands to large shear strains (>3). Thus, it is not necessary to invoke non-Newtonian viscosity to account for the melt-rich bands forming at ~15°. In experiments, segregation occurs and bands stabilize at low angles in samples deformed at very different stress levels, from low stresses well within the diffusion creep-dominated regime, to higher stresses within the dislocation creep regime. Although all samples developed an olivine fabric (implying that dislocation creep was active), the experimental samples had a range of effective stress exponents, from 1 to >4.5, consistent with the stress conditions. Therefore, the segregation and organization are not sensitive to the stress exponent in the matrix, favoring the viscous anisotropy mechanism.

[59] However, there are complications in applying the results of the linear stability analysis directly to the experiments. At strains >1, the grain-scale melt alignment was closer to the case B form (22.5° to the shear plane) than the case A end-member (45°). As shown in Figure 12, case B anisotropy tends to favor the stability of the higher angle bands. Therefore, we conclude that at onset of deformation, the initial melt pocket orientation is closer to case A, and the anisotropic viscosity is the predominant cause for band formation. We suggest that, as the system evolves, other processes come into play that tend to enhance strain localization in the bands and favor the low angles. These processes could include stress-dependent (non-Newtonian) mechanisms as discussed by *Katz et al.* [2006] and the requirements for steady state strain partitioning [*Holtzman et al.*, 2005].

[60] Although the present theory is based on viscous rheology insensitive to confining pressure, the obtained low-angle localization is phenomenologically similar to localization that occurs in dilatent granular or brittle/frictional materials in a wide range of mechanical regimes (often called "Reidel shears" [e.g., *Schmocker et al.*, 2003]). It seems worth investigating whether there is a universality to the low-angle localization, and that interactions between a wide range of mechanisms find a similar balance between shear and normal stresses.

7. Discussion

[61] The present results, showing the occurrence of melt migration up stress gradients and the formation of low-angle melt rich bands, demonstrate the significant effects of viscous anisotropy on melt migration dynamics: stress-induced melt alignment at the grain scale drives further melt redistribution over distances much longer than the grain scale. While spontaneous segregation into melt-rich bands occurs over distances smaller than the compaction length, melt migration up stress gradients can occur over distances greater than the compaction length. These two mechanisms imply the development of multiscale rheological structure, ranging from grain scale to mesoscale or global scale. (Schematic illustrations and terminology for multiscale structure are presented in Figures 12 and 14 of

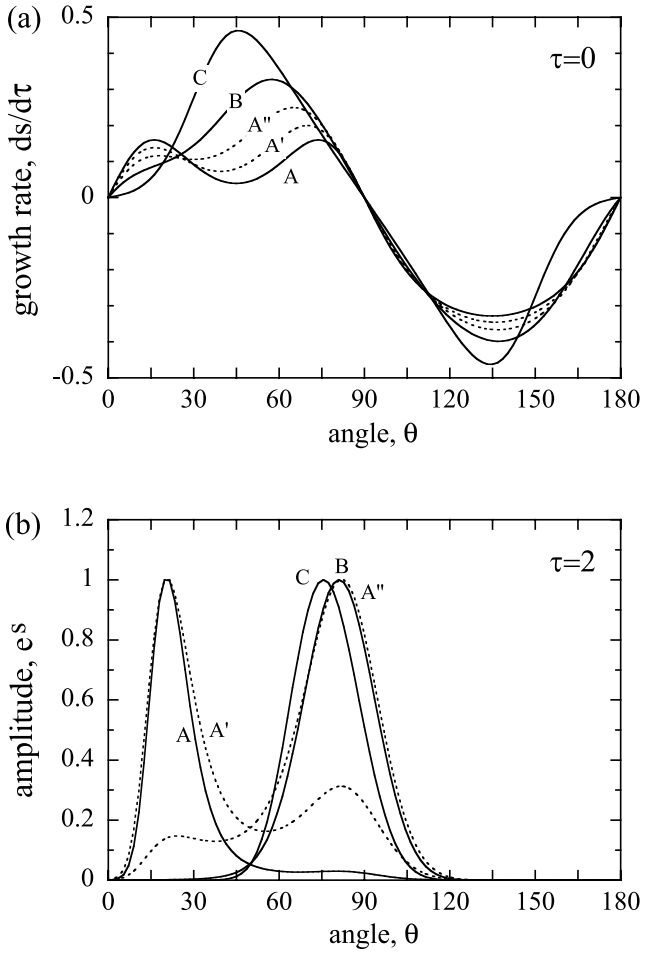

Figure 12. (a) Growth rate $ds/d\tau$ versus θ at $\tau = 0$ calculated for anisotropic geometry of cases A, B, and C (Figures 2c–2e) and two intermediate cases between A and B (labeled A′ and A″). $(\Theta_1, \Theta_2) = (0.1,0.3)$ for A, (0.13, 0.27) for A′, (0.16, 0.24) for A″, (0.2, 0.2) for B, and (0.3, 0.1) for C, where $\Theta_3 = \Theta_4 = 0.3$ for all cases. These correspond to the melt alignment at 45° (A), 38° (A′), 31.5° (A″), 22.5° (B) and 0° (C) angles to the shear plane. (b) Amplitude e^s versus θ at $\tau = 2$, where amplitude is normalized to the maximum value of each line. Low-angle bands develop for A and A′, and high-angle bands develop for A″, B, and C.

TH1.) In sections 5 and 6, we considered only initial evolutions or small perturbations of the porosity structures to obtain exact and self-consistent solutions. Here, by introducing several assumptions and approximations, we discuss the geodynamical applications and implications of the present results.

7.1. Effective Viscosity and Lubrication

[62] In this study, for mathematical simplicity, we have compared the influence of deformation on melt migration in two simple and definable systems: the initial evolution of porosity in rotary shear and the growth of small perturbations of porosity in simple shear. In so doing, we have analyzed in detail the influence of deformation on melt migration, but not the feedbacks from the evolving melt distribution to the boundary conditions or effective viscosity of the system. For example, as melt migrates up a stress gradient, it modifies the viscosity structure internal to the system. In the constant torque system discussed in section 5, viscosity reduction in the inner radii causes strain localization, which will feedback to the boundary conditions; the velocity will increase to maintain a constant torque. This increase in velocity is quantified as an effective viscosity, and the process referred to as lubrication. Such lubrication may occur in various settings in the Earth, with significant dynamic consequences. Solving the fully nonlinear time-dependent problem is beyond the scope of this study, but here we present a simple snapshot view of the effective viscosity of an evolved system in which melt has segregated toward a boundary. Determining an effective viscosity for the melt-rich band structures at an angle to the shear plane is difficult because the partitioning of stress and strain must be considered [e.g., *Holtzman et al.*, 2005]. This problem is left for future studies. Here, we discuss the effective viscosity of the rotary shear model.

[63] We consider a concentric structure consisting of two homogeneous parts with porosity ϕ_{in} and viscosity η_{in} at $a \le r \le c$ and ϕ_{out} and η_{out} at $c \le r \le b$, where the inner part has larger porosity (Figure 13a). This structure reflects the consequence of melt migration up stress gradients in the solid matrix. For simplicity, the viscosity within each part is assumed to be isotropic. For comparison, we also consider a simple shear of the system consisting of two homogeneous parts with ϕ_{in} and η_{in} at $0 \le y \le c$ and ϕ_{out} and η_{out} at $c \le y \le b$ (Figure 13b). Let S_{in} and S_{out} be the areas of the inner and outer parts and let S_{total} be $S_{in} + S_{out}$. Let $\bar{\phi}$ be average porosity, which is defined by $S_{total}\bar{\phi} = S_{in}\phi_{in} + S_{out}\phi_{out}$. Effective viscosity, η_{eff}, for rotary or simple shear is given as

Rotary shear

$$\frac{\eta_{eff}}{\bar{\eta}} = \frac{\bar{\eta}^{-1}c^2(b^2 - a^2)}{\eta_{in}^{-1}b^2(c^2 - a^2) + \eta_{out}^{-1}a^2(b^2 - c^2)} \tag{56a}$$

Simple shear

$$\frac{\eta_{eff}}{\bar{\eta}} = \frac{\bar{\eta}^{-1}b}{\eta_{in}^{-1}c + \eta_{out}^{-1}(b - c)} \tag{56b}$$

where $\bar{\eta}$ represents the viscosity of the homogeneous system with $\bar{\phi}$. In TH1, shear viscosity is obtained as a function of grain boundary contiguity φ as $\eta = 0.2\eta_{cc}\varphi^2$, where φ is related to melt fraction ϕ as $\varphi = 1 - A\phi^{1/2}$ with $A = 2$–2.3. Here, we use the result of the contiguity model rather than the exponential dependence used in section 6, because the viscosity at large ϕ is better described by the contiguity model. With $A = 2.3$, both contiguity φ and viscosity η become zero at $\phi = 0.189$. This is realistic, because viscosity at $\varphi = 0$ is controlled by the liquid viscosity, which is negligibly small compared to the solid viscosity. The melt fraction corresponding to $\varphi = 0$ ($\phi = 0.189$ for $A = 2.3$) is sometimes called the rheologically critical melt fraction (RCMF). (Not to be confused with ϕ_c of TH1 and TH2.)

[64] Figures 13c and 13d show ϕ_{in} versus ϕ_{out} and η_{eff} versus ϕ_{out} for various values of S_{in}/S_{total}, where $\bar{\phi}$ is fixed

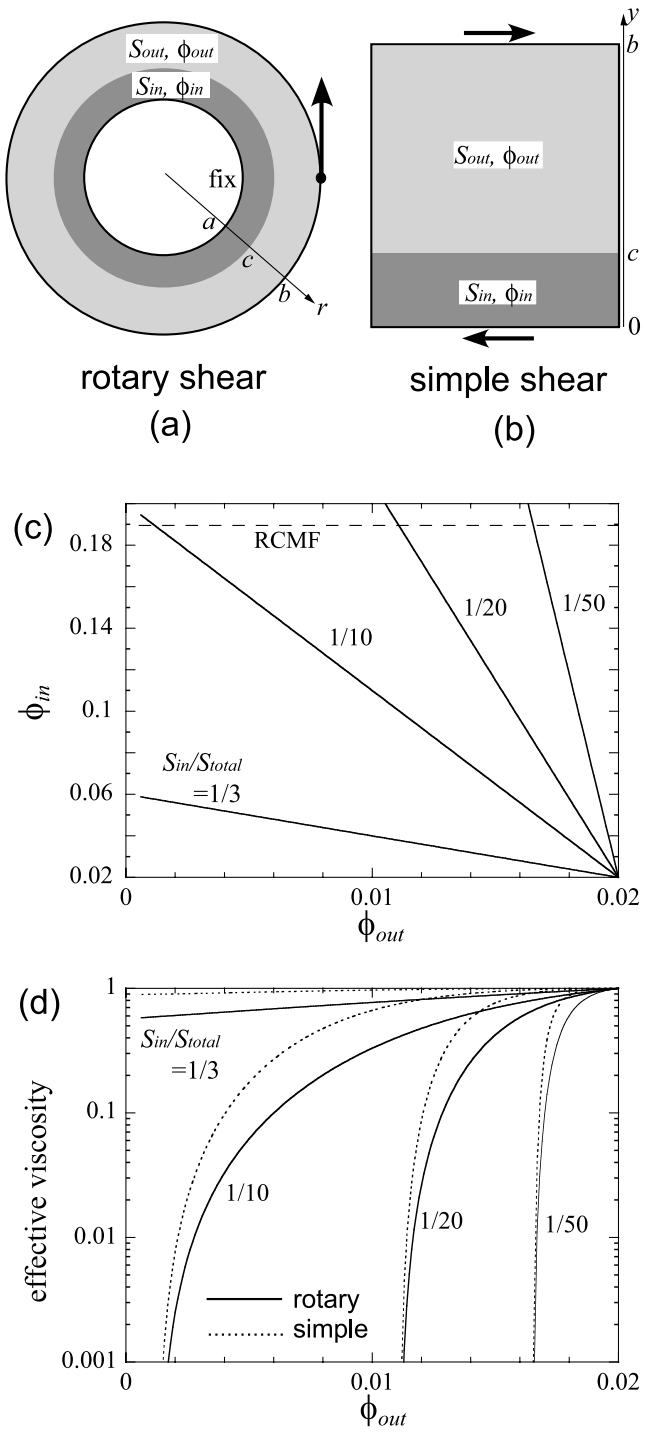

Figure 13. (a, b) Rotary and simple shear models consisting of the two parts characterized by porosity ϕ_{in} and area S_{in} (darkly shaded region) and ϕ_{out} ($<\phi_{in}$) and S_{out} (lightly shaded region). (c) The parameter ϕ_{in} versus ϕ_{out} for various S_{in}/S_{total}, where average melt fraction is fixed to $\bar{\phi}$ = 0.02. (d) Effective viscosity for rotary shear model (solid lines) and simple shear model (dotted lines), normalized to the viscosity corresponding to $\bar{\phi}$ = 0.02.

to be 0.02. The η_{eff} is dominantly influenced by the smaller viscosity, η_{in}. Therefore, as ϕ_{in} approaches 0.189, η_{in} approaches zero and η_{eff} accordingly decreases toward zero, illustrating the process of lubrication. Figure 13d shows that the lubrication significantly depends on S_{in}/S_{total}, which describes the spatial localization of the segregation. The result of section 5 shows that the configuration of segregation is controlled by the ratio of the magnitude of the spatial scale of the shear stress gradient (b) and the compaction length (δ_c); by roughly approximating S_{in} and S_{out} by the areas where decompaction and compaction occur, respectively, S_{in}/S_{total} is estimated as 0.38 for δ_c/b = 0.5, 0.047 for δ_c/b = 0.01, and 0.008 for δ_c/b = 0.001. The detailed configuration of segregation may also be affected by the dependence of anisotropy on the shear stress amplitude. Figure 13d shows that because of the heterogeneity in stress, the lubrication effect on η_{eff} at a given ϕ_{out} is larger for the rotary shear (solid lines) than for the simple shear (dotted lines).

[65] These results indicate the importance of further investigating the effects of melt migration up stress gradients for realistic material properties and geological settings. In section 7.2, we discuss melt migration up stress gradients in the context of the mantle at ridges and subduction zones.

7.2. Geodynamic Consequences of Anisotropic Viscosity and Lubrication

[66] Previous studies on the two-phase dynamics of partially molten regions have been performed only for isotropic viscosity. Even for an isotropic viscosity, fully solving the solid-liquid two-phase dynamics is not an easy task. In order to estimate fluid flow at ridges and subduction zones, *Spiegelman and McKenzie* [1987] proposed a simple model in which the liquid pressure gradient is calculated from equation (29) using analytical solutions of $\mathbf{v}^S$ obtained under the assumption of constant porosity. We applied their simple model to the rotary shear system with anisotropic viscosity and showed that, when $\delta_c/b \ll 1$, liquid pressure gradient can be closely approximated by the simple model (section 5.4.2). Here, by considering that the compaction length is much smaller than the spatial scale of the mantle flow, effects of viscous anisotropy on melt streamlines are estimated by the simple model.

[67] The flow of mantle at spreading centers and subduction zones is modeled by 2-D corner flow which can be solved analytically with isotropic viscosity [e.g., *Spiegelman and McKenzie*, 1987]. We estimate melt streamlines at both settings by approximating solid velocity $\mathbf{v}^S$ with these analytical solutions, in combination with the viscosity tensor calculated for stress-induced anisotropy of case A. Similar to the rotary shear system, stress and strain rate of the corner flow with isotropic viscosity have only $r\theta$ (and θr) components. So, as discussed in section 5.4.2, the viscous constitutive relation given by equation (17) is used. Further details of the calculation are presented in Appendix C.

[68] The melt and matrix streamlines at ridges and subduction zones are shown in Figures 14 and 15. In Figures 14 and 15, length, time, and stress are normalized to L, L/U_0, and $\eta_0 U_0/L$, respectively, where U_0 is half spreading rate or subduction rate and η_0 is isotropic shear viscosity of the matrix. L is defined by (C5) and is estimated as about 3–30 km for $\eta - \zeta_1 = 10^{19}$–10^{21} Pa s (Appendix C). With isotropic viscosity, melt streamlines near the spreading center are focused on the singular point (dotted lines in Figure 14b), while with anisotropic viscosity, the stream-

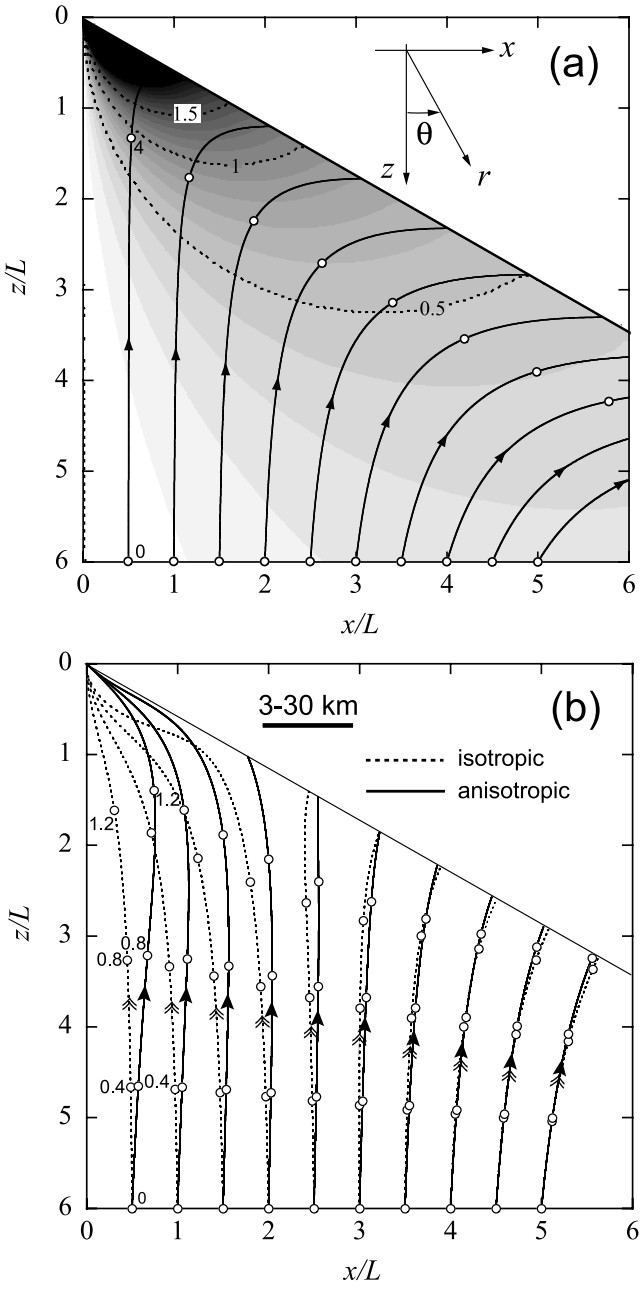

Figure 14. Effects of anisotropic viscosity on melt flow in a mid-ocean ridge model. (a) Solid streamlines (solid lines) with circles showing the position at every normalized time step 4 starting from $z/L = 6$. Amplitude of shear stress $(\sigma^B_{r\theta})_0$ is shown by the gray scale with a contour of 0.5 (dotted lines). (b) Melt streamlines estimated for isotropic viscosity (dotted lines) and for anisotropic viscosity (solid lines). Circles show the position at every normalized time step 0.4 starting from $z/L = 6$. Spreading center is at the origin. Factors used for normalization of length, time, and stress are given in the text.

lines curve outward (solid lines in Figure 14b), because the large shear stresses along the dipping plate boundary (dark region in Figure 14a) pull melt toward the boundary. A similar result is also obtained for the subduction model. With isotropic viscosity, liquid can migrate upward from the slab surface due to the dominant effect of buoyancy force (dotted lines in Figure 15b). However, with anisotropic viscosity, the liquid is attracted to the surface of the subducting slab due to migration up stress gradients (solid lines in Figure 15b).

[69] What are the implications of these simple solutions for the complex dynamics of the mantle at the spreading and convergent plate boundaries? In both cases, the melt attracted to the plate boundaries is expected to reduce viscosity and lubricate the plate motion. Because viscosity

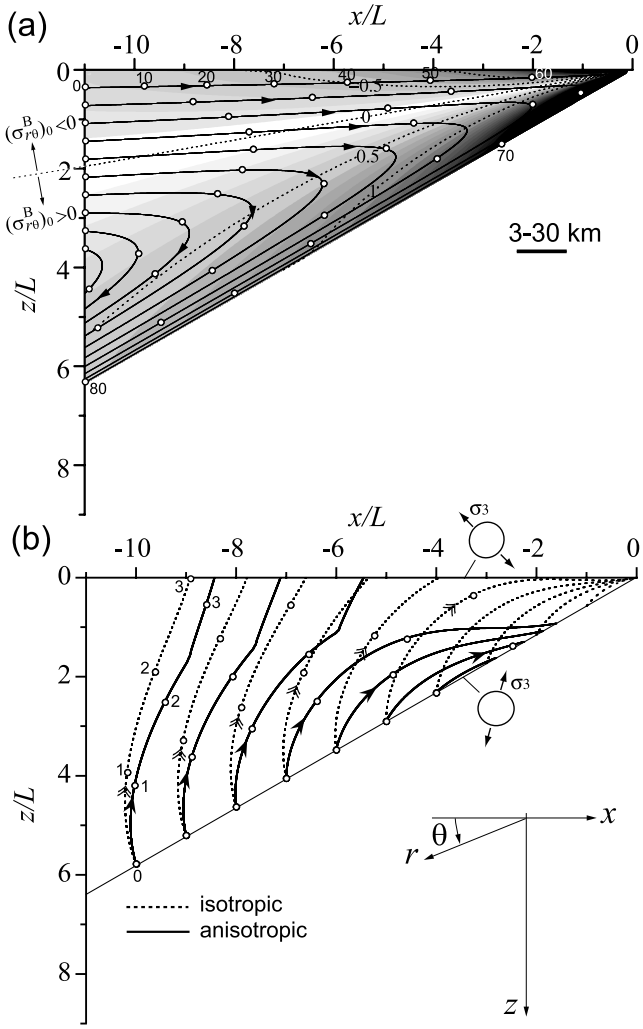

Figure 15. Effects of anisotropic viscosity on melt flow in a subduction zone model. (a) Solid streamlines (solid lines) with circles showing the position at every normalized time step 10 starting from $x/L = -11$. Amplitude of shear stress $|(\sigma^B_{r\theta})_0|$ is shown by the gray scale with a contour of 0.5 (dotted lines). (b) Melt streamlines estimated for isotropic viscosity (dotted lines) and for anisotropic viscosity (solid lines). Circles show the position at every normalized time step 1 starting from the surface of the subducting plate. The σ_3 direction at $\theta = 0°$ (surface) and $\theta = 30°$ (slab surface) is shown in Figure 15b. Factors used for normalization of length, time, and stress are given in the text.

reduction changes the matrix stress field and hence affects the melt streamlines, dynamic approaches that take into account interactions or feedbacks between melt migration and mantle flow should be performed in future studies. Although we considered a passive corner flow model for simplicity, buoyancy force of the upwelling mantle provides an additional driving force, especially at spreading plate boundaries. The driving forces of the plate motion affect the stress field and hence affect the melt migration patterns. Therefore, dynamic approaches with realistic driving forces are important. The occurrence of lubrication may be tested by the observation and characterization of seismic low-velocity zones and/or seismic anisotropy. The possible occurrence of lubrication and its seismological detectability in the suboceanic upper mantle are discussed by TH1. In subduction zones, the degree and depth of decoupling (or lubrication) between the subducting plate and the mantle wedge exerts a primary control on the thermal structure of the mantle wedge [e.g., *Furukawa*, 1993] and with a more macroscopic view, the fundamental asymmetry of the subduction geometry [*Gerya et al.*, 2008]. Many subduction zones exhibit low-velocity waveguides several kilometers thick in the vicinity of the Wadati-Benioff zone and the slab interface [e.g., *Abers*, 2005]. Their origin is not clear, but slab-derived fluids and possibly melts could be responsible for their low seismic velocities. In experiments, stress causes a similar alignment of aqueous fluids in an ultramafic matrix [*Hier-Majumder and Kohlstedt*, 2006] as is observed in partially molten ultramafic systems. If the presence and alignment of fluids have similar effects on the rheology of the systems of ultramafic matrix/aqueous fluids at mantle wedge conditions, then the coupling between shear and isotropic stresses developed here could occur in such systems. In the Earth's mantle, dislocation creep is also an important deformation mechanism, so a relevant viscous constitutive relation should incorporate it. Effects of aqueous fluids should also be considered in future studies.

8. Conclusions

[70] With viscous anisotropy, the influence of shear deformation on melt migration significantly increases, because viscous anisotropy causes a direct coupling between shear and isotropic components, which does not occur with isotropic viscosity. Significant consequences of this coupling are demonstrated by two simple models: the occurrence of melt migration up stress gradients in the solid matrix was demonstrated by a rotary shear model; the formation of melt-rich bands was demonstrated by linear stability analysis of a simple shear model, with results consistent with experimental observation. Effects of viscous anisotropy on melt migration was demonstrated in two geological settings by approximating mantle flow at spreading centers and subduction zones with analytical solutions for corner flow. Migration of melt up stress gradients may drive segregation toward the lithosphere-asthenosphere boundary and slab surface in ridges and subduction zones, respectively.

[71] Stress-induced melt alignment at the grain scale causes viscous anisotropy, which further drives melt redistribution over distances greater than the grain scale. The present study demonstrates the development of such multiscale anisotropy by forward or ab initio approaches based on the governing equations of two-phase dynamics. While spontaneous segregation into melt-rich bands occurs over distances smaller than the compaction length, melt migration up stress gradients can occur over distances greater than the compaction length. The viscous macroscopic constitutive relation based on realistic microstructures and grain-scale rheology plays an important role as a bridge between microscopic and macroscopic processes. The development of multiscale structures can cause both increased permeability and significant weakening and lubrication at geodynamic scales. In addition to the viscous constitutive relation in the regime of grain boundary diffusion creep derived in this study, further studies are needed for dislocation creep, where viscous anisotropy can be produced not only by grain-scale melt alignment but also by lattice preferred orientation (LPO).

Appendix A: Anisotropic Viscosity for Incompressible Flow

[72] The viscous constitutive relation for incompressible flow in two dimensions is generally written as

$$\begin{pmatrix} \sigma^B_{xx} - \frac{\sigma^B_{xx}+\sigma^B_{yy}}{2} \\ \sigma^B_{yy} - \frac{\sigma^B_{xx}+\sigma^B_{yy}}{2} \\ \sigma^B_{xy} \\ \sigma^B_{yx} \end{pmatrix} = \begin{pmatrix} D_1 + D_2 & D_2 & D_3 & D_3 \\ D_2 & D_1 + D_2 & -D_3 & -D_3 \\ D_3 & -D_3 & D_4 & D_4 \\ D_3 & -D_3 & D_4 & D_4 \end{pmatrix} \begin{pmatrix} \dot{\varepsilon}^f_{xx} \\ \dot{\varepsilon}^f_{yy} \\ \dot{\varepsilon}^f_{xy} \\ \dot{\varepsilon}^f_{yx} \end{pmatrix}, \tag{A1}$$

where $\dot{\varepsilon}^f_{xx} + \dot{\varepsilon}^f_{yy} = 0$ and D_2 in the matrix is an arbitrary constant. An important difference between equation (9) and equation (A1) lies in the off-diagonal quadrants, which negates the possibility of coupling between shear and isotropic components.

Appendix B: Model of *Katz et al.* [2006]

[73] Here, we present the model of *Katz et al.* [2006] developed for the system with isotropic and nonlinear viscosity. Our rederivation gives a growth rate which is quantitatively different from that of *Katz et al.* [2006].

[74] Using the notations of this present study, the nonlinear flow law reported from experimental studies can be written as

$$\dot{\varepsilon}^f_{xy} = ce^{\lambda\phi} \left| \frac{\sigma^B_{xy}}{\mu} \right|^{n-1} \frac{\sigma^B_{xy}}{\mu}, \tag{B1}$$

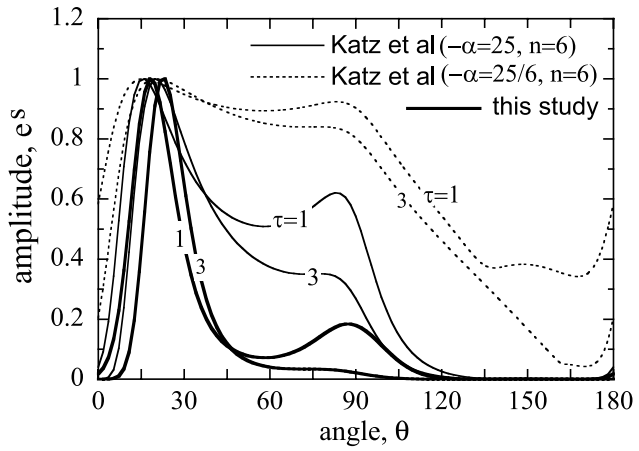

Figure B1. Amplitude e^s versus θ at $\tau = 1$ and 3, predicted from the model of *Katz et al.* [2006] and from the model of this study (thick lines). Amplitude is normalized to the maximum value at each τ. The results of the model of *Katz et al.* [2006] are shown both for the parameter values similar to their original values ($(1-\phi^0)\lambda/n = 25$, $n = 6$, and $\xi^0/\eta^0 = 10$; solid lines) and for the modified values ($(1-\phi^0)\lambda/n = 25/6$, $n = 6$, and $\xi^0/\eta^0 = 10$; dotted lines).

where μ and c are constants with dimensions of Pa and s^{-1}, respectively, and $\lambda \simeq 25-37$ [*Mei et al.*, 2002; *Zimmerman and Kohlstedt*, 2004]. Equation (B1) can be rewritten as

$$\sigma^B_{xy} = \mu e^{-\frac{\lambda}{n}\phi} \left| \frac{\dot{\varepsilon}^f_{xy}}{c} \right|^{\frac{1}{n}-1} \frac{\dot{\varepsilon}^f_{xy}}{c}. \tag{B2}$$

For a small perturbation in melt fraction, $\phi = \phi^0 + \epsilon\phi^1$, equation (B2) becomes

$$\sigma^{B0}_{xy} + \epsilon\sigma^{B1}_{xy} = \sigma^{B0}_{xy}\left(1 - \epsilon\frac{\lambda}{n}\phi^1 + \epsilon\frac{1-n}{n}\frac{\dot{\varepsilon}^{f1}_{xy}}{\dot{\varepsilon}^{f0}_{xy}} + \epsilon\frac{\dot{\varepsilon}^{f1}_{xy}}{\dot{\varepsilon}^{f0}_{xy}}\right). \tag{B3}$$

Because the perturbation in stress can be expressed using linearized viscosity, $\eta = \eta^0 + \epsilon\eta^1$, as

$$\sigma^{B0}_{xy} + \epsilon\sigma^{B1}_{xy} = \sigma^{B0}_{xy}\left(1 + \epsilon\frac{\dot{\varepsilon}^{f1}_{xy}}{\dot{\varepsilon}^{f0}_{xy}} + \epsilon\frac{\eta^1}{\eta^0}\right), \tag{B4}$$

by comparing equations (B3) and (B4), we obtain

$$\frac{\eta^1}{\eta^0} = -\frac{\lambda}{n}\phi^1 + \frac{1-n}{n}\frac{\dot{\varepsilon}^{f1}_{xy}}{\dot{\varepsilon}^{f0}_{xy}}. \tag{B5}$$

Through the comparison between equation (B5) and equation (S10) of *Katz et al.* [2006], we can see that the parameter α used by *Katz et al.* [2006] corresponds to $-\lambda/n$.

[75] Decompaction C and rotation Ω for the non-Newtonian model can be obtained from the same equation as equations (47) and (54) by replacing Δ_{ij} with

$$\begin{cases} \Delta_{11} = 4\frac{1-n}{n}n_x^2 n_y^2 \\ \Delta_{12} = \Delta_{21} = 2\frac{1-n}{n}n_x n_y (n_y^2 - n_x^2) \\ \Delta_{22} = \frac{1-n}{n}(n_x^2 - n_y^2)^2, \end{cases} \tag{B6}$$

which vanish when $n = 1$. Then, the growth rate $ds/d\tau$ is obtained as

$$\frac{ds}{d\tau} = 2\frac{\lambda}{n}\cdot\frac{(1-\phi^0)n_x n_y}{\frac{\xi^0+\eta^0}{\eta^0}\left(1+\frac{1}{K^2}\right)\left(1+\frac{1-n}{n}(n_x^2-n_y^2)^2\right)+\frac{1-n}{n}4n_x^2 n_y^2}, \tag{B7}$$

which is equal to the result of *Katz et al.* [2006, equation S23], if $\lambda/n = -\alpha$. (As discussed in section 6.1.2, a slight difference of factor $\eta^0/(\xi^0 + \eta^0)$ in equation (B7) from $\xi = \eta_0/(\zeta_0 + 4\eta_0/3)$ from *Katz et al.* [2006] comes from our use of the viscous constitutive relation derived in two dimensions.)

[76] Equation (B5) shows that as the nonlinearity n increases, the porosity weakening effect given by the first term of the right-hand side decreases as λ/n. Although *Katz et al.* [2006, equation S10] used $-\alpha = 27$ even for $n = 6$, our result shows that $-\alpha$ is $\sim$7 for $n = 4$ and $\sim$5 for $n = 6$. The values of $\alpha = -27$ and $n = 6$ used in *Katz et al.* [2006] overestimate the effect of melt fraction. Amplitude $e^{s(\theta,\tau)}$ versus θ is shown in Figure B1, where the results of the model of *Katz et al.* [2006] are shown for the parameter values similar to their original values (solid lines) and for the values corrected for the overestimation (dotted lines).

Appendix C: Melt Streamlines in the Corner Flow Ridge and Trench Models

[77] In the simple model developed by *Spiegelman and McKenzie* [1987], solid velocity $\mathbf{v}^S$ is approximated by the analytical solutions for passive corner flow. For the ridge model, $\mathbf{v}^S$ is given by

$$\begin{cases} \frac{v_r^S}{U_0} = C_R\cos\theta - D_R(\cos\theta - \theta\sin\theta) \\ \frac{v_\theta^S}{U_0} = -C_R\sin\theta + D_R\theta\cos\theta, \end{cases} \tag{C1}$$

where $C_R = 2\sin^2\alpha/(\pi - 2\alpha - \sin 2\alpha)$ and $D_R = 2/(\pi - 2\alpha - \sin 2\alpha)$ for wedge angle α, and U_0 is the half spreading rate [*Spiegelman and McKenzie*, 1987]. For the trench model, $\mathbf{v}^S$ is given by

$$\begin{cases} \frac{v_r^S}{U_0} = C_T\theta\sin\theta + D_T(\sin\theta + \theta\cos\theta) \\ \frac{v_\theta^S}{U_0} = -C_T(\sin\theta - \theta\cos\theta) - D_T\theta\sin\theta, \end{cases} \tag{C2}$$

where $C_T = \beta\sin\beta/(\beta^2 - \sin^2\beta)$ and $D_T = (\beta\cos\beta - \sin\beta)/(\beta^2 - \sin^2\beta)$ for wedge angle β, and U_0 is the subduction rate [*Spiegelman and McKenzie*, 1987]. Coordinate systems are defined in Figures 14 and 15, where θ is defined differently between the two models. The strain rate calculated by substituting equation (C1) (or (C2)) into equation (4) has only $r\theta$ (and θr) component ($\dot{\varepsilon}^f_{rr} = \dot{\varepsilon}^f_{\theta\theta} = 0$). In the cylindrical coordinate system, equation (16) is written as

$$\begin{cases} \frac{\partial p^L}{\partial r} = (\sigma^B_{rr} + p^L)_{,r} + \frac{1}{r}\sigma^B_{r\theta,\theta} + \frac{\sigma^B_{rr}-\sigma^B_{\theta\theta}}{r} + \bar{\rho}g_r \\ \frac{1}{r}\frac{\partial p^L}{\partial\theta} = \sigma^B_{r\theta,r} + \frac{1}{r}(\sigma^B_{\theta\theta} + p^L)_{,\theta} + \frac{2}{r}\sigma^B_{r\theta} + \bar{\rho}g_\theta, \end{cases} \tag{C3}$$

where g_r and g_θ are the r and θ components of the gravitational acceleration. By substituting equations (15) and (17) into equations (C3) and by using $\dot{\varepsilon}^f_{rr} = \dot{\varepsilon}^f_{\theta\theta} = 0$, liquid velocity $\mathbf{v}^L$ is obtained as

$$\begin{cases} \frac{v^L_r}{U_0} = \frac{v^S_r}{U_0} - \frac{w}{U_0}\frac{g_r}{g} + \frac{wL^2}{U_0^2}\left[2\gamma\dot{\varepsilon}^f_{r\theta,r} - \frac{2}{r}\dot{\varepsilon}^f_{r\theta,\theta}\right] \\ \qquad + \frac{wL^2}{U_0^2}2\dot{\varepsilon}^f_{r\theta}\left[\gamma_{,r} + \frac{1}{\eta-\zeta_1}\left\{\gamma(\eta-\zeta_1)_{,r} - \frac{1}{r}(\eta-\zeta_1)_{,\theta}\right\}\right] \\ \frac{v^L_\theta}{U_0} = \frac{v^S_\theta}{U_0} - \frac{w}{U_0}\frac{g_\theta}{g} + \frac{wL^2}{U_0^2}\left[-2\dot{\varepsilon}^f_{r\theta,r} + \frac{2\gamma}{r}\dot{\varepsilon}^f_{r\theta,\theta} - \frac{4}{r}\dot{\varepsilon}^f_{r\theta}\right] \\ \qquad + \frac{wL^2}{U_0^2}2\dot{\varepsilon}^f_{r\theta}\left[\frac{\gamma_{,\theta}}{r} + \frac{1}{\eta-\zeta_1}\left\{-(\eta-\zeta_1)_{,r} + \frac{\gamma}{r}(\eta-\zeta_1)_{,\theta}\right\}\right], \end{cases} \tag{C4}$$

where w and L are given by

$$\begin{cases} w = \frac{k_\phi(1-\phi)\Delta\rho g}{\eta_L \phi} \\ L = \left(\frac{U_0(\eta-\zeta_1)}{(1-\phi)\Delta\rho g}\right)^{1/2}. \end{cases} \tag{C5}$$

For $U_0 = 7.5$ cm a^{-1}, $\Delta\rho = 300$ kg m^{-3}, $g = 9.8$ m s^{-2}, $\phi = 0.03$, $\eta - \zeta_1 = 10^{19}$–10^{21} Pa s, L is estimated as about 3–30 km.

[78] Let $(\sigma^B_{r\theta})_0$ be the shear stress field of the corner flow with isotropic viscosity, which is given by $(\sigma^B_{r\theta})_0 = \eta_0\,\dot{\varepsilon}^f_{r\theta}$ by using η_0 defined in section 3.4. The γ and $\eta - \zeta_1$ are given by smooth functions of $(\sigma^B_{r\theta})_0$ as

$$\gamma = \begin{cases} \gamma_{sat}\sin\left(\frac{\pi}{2}\frac{(\sigma^B_{r\theta})_0}{\sigma_{sat}}\right) & \text{at } |(\sigma^B_{r\theta})_0| \le \sigma_{sat} \\ \gamma_{sat}\frac{(\sigma^B_{r\theta})_0}{|(\sigma^B_{r\theta})_0|} & \text{at } |(\sigma^B_{r\theta})_0| > \sigma_{sat} \end{cases} \tag{C6}$$

and

$$\frac{\eta-\zeta_1}{\eta_0} = \begin{cases} \frac{1-c_{sat}}{2}\cos\left(\pi\frac{(\sigma^B_{r\theta})_0}{\sigma_{sat}}\right) + \frac{1+c_{sat}}{2} & \text{at } |(\sigma^B_{r\theta})_0| \le \sigma_{sat} \\ c_{sat} & \text{at } |(\sigma^B_{r\theta})_0| > \sigma_{sat}, \end{cases} \tag{C7}$$

where $(\sigma^B_{r\theta})_0$ can be both $(\sigma^B_{r\theta})_0 \ge 0$ and $(\sigma^B_{r\theta})_0 < 0$, and σ_{sat} (>0) represents the saturation limit above which the anisotropy becomes independent of the stress magnitudes. Using the result shown in Figure 4, $\gamma_{sat} = 0.988$ and $c_{sat} = 0.51$. Substituting equations (C1) (or (C2)) and (C6)–(C7) into equations (C4), melt streamlines shown in Figures 14 and 15 are obtained. In Figures 14 and 15, $\alpha = \beta = \pi/6$, $w/U_0 = 1.91$, and $\sigma_{sat}/(\eta_0 U_0/L) = 0.03$ are used. With this value of σ_{sat}, stress-induced anisotropy is saturated in most parts of the domain except for the vicinity of the region of $(\sigma^B_{r\theta})_0 = 0$, which extends along a line of $\theta = 0$ in the ridge model and a line of $\theta = 0.178$ rad in the trench model. The patterns of streamlines discussed in section 7.2 are not sensitive to the value of σ_{sat}.

[79] Although equation (17) corresponding to the anisotropy of case A is used in deriving equations (C4), because $\dot{\varepsilon}^f_{rr} = \dot{\varepsilon}^f_{\theta\theta} = 0$, the same result is obtained from equation (9). Therefore, similar streamlines to Figures 14 and 15 can be obtained for both cases A and B.

[80] **Acknowledgments.** We would like to thank M. Spiegelman and R. Katz for stimulating discussions and J. Phipps Morgan for his supportive pressure. We also thank Reid Cooper and an anonymous reviewer for their thoughtful comments that helped to improve the paper. The International Office at ERI generously supported the visits of B.K.H.

References

Abers, G. A. (2005), Seismic low-velocity layer at the top of subducting slabs: Observations, predictions, and systematics, *Phys. Earth Planet. Inter.*, *149*, 7–29.

Christensen, U. R. (1987), Some geodynamical effects of anisotropic viscosity, *Geophys. J. R. Astron. Soc.*, *91*, 711–736.

Daines, M. J., and D. L. Kohlstedt (1997), Influence of deformation on melt topology in peridotites, *J. Geophys. Res.*, *102*, 10,257–10,271.

Furukawa, Y. (1993), Depth of the Decoupling Plate Interface and Thermal Structure Under Arcs, *J. Geophys. Res.*, *98*, 20,005–20,013.

Gerya, T. V., J. A. D. Connolly, and D. A. Yuen (2008), Why is terrestrial subduction one-sided?, *Geology*, *36*, 43–46.

Gourlay, C. M., and A. K. Dahle (2005), Shear deformation at 29% solid during solidification of magnesium alloy AZ91 and aluminium alloy A356, *Mater. Sci. Eng. A*, *413–414*, 180–185.

Hier-Majumder, S., and D. L. Kohlstedt (2006), Role of dynamic grain boundary wetting in fluid circulation beneath volcanic arcs, *Geophys. Res. Lett.*, *33*, L08305, doi:10.1029/2006GL025716.

Holtzman, B. K., and D. L. Kohlstedt (2007), Stress-driven melt-segregation and strain partitioning in partially molten rocks: Effects of stress and strain, *J. Petrol.*, *48*, 2379–2406.

Holtzman, B. K., N. J. Groebner, M. E. Zimmerman, S. B. Ginsberg, and D. L. Kohlstedt (2003a), Stress-driven melt segregation in partially molten rocks, *Geochem. Geophys. Geosyst.*, *4*(5), 8607, doi:10.1029/2001GC000258.

Holtzman, B. K., D. L. Kohlstedt, M. E. Zimmerman, F. Heidelbach, T. Hiraga, and J. Hustoft (2003b), Melt segregation and strain partitioning: Implications for seismic anisotropy and mantle flow, *Science*, *301*, 1227–1230.

Holtzman, B. K., D. L. Kohlstedt, and J. Phipps Morgan (2005), Viscous energy dissipation and strain partitioning in partially molten rocks, *J. Petrol.*, *46*, 2569–2592.

Honda, S. (1986), Strong anisotropic flow in a finely layered asthenosphere, *Geophys. Res. Lett.*, *13*, 1454–1457.

Iwamori, H. (1994), ^{238}U-^{230}Th-^{226}Ra and ^{235}U-^{231}Pa disequilibria produced by mantle melting with porous and channel flows, *Earth Planet. Sci. Lett.*, *125*, 1–16.

Katz, R. F., M. Spiegelman, and B. K. Holtzman (2006), The dynamics of melt and shear localization in partially molten aggregates, *Nature*, *442*, 676–679, doi:10.1038/nature05039.

Kelemen, P. B., G. Hirth, N. Shimizu, M. Spiegelman, and H. J. B. Dick (1997), A review of melt migration processes in the adiabatically upwelling mantle beneath oceanic spreading ridges, *Philos. Trans. R. Soc. London, Ser. A*, *355*, 283–318.

Lev, E., and B. H. Hager (2008), Rayleigh-Taylor instabilities with anisotropic lithospheric viscosity, *Geophys. J. Int.*, *173*, 806–814, doi: 10.1111/j.1365-246X.2008.03731.x.

McKenzie, D. (1984), The generation and compaction of partially molten rock, *J. Petrol.*, *25*, 713–765.

Mei, S., W. Bai, T. Hiraga, and D. L. Kohlstedt (2002), Influence of melt on the creep behavior of olivine-basalt aggregates under hydrous conditions, *Earth Planet. Sci. Lett.*, *201*, 491–507.

Phipps Morgan, J. (1987), Melt migration beneath mid-ocean spreading centers, *Geophys. Res. Lett.*, *14*, 1238–1241.

Saito, M., and Y. Abe (1984), Consequences of anisotropic viscosity in the Earth's mantle (in Japanese), *J. Seismol. Soc. Jpn.*, *37*, 237–245.

Schmocker, M., M. Bystricky, K. Kunze, L. Burlini, H. Stünitz, and J.-P. Burg (2003), Granular flow and Riedel band formation in water-rich quartz aggregates experimentally deformed in torsion, *J. Geophys. Res.*, *108*(B5), 2242, doi:10.1029/2002JB001958.

Spiegelman, M. (2003), Linear analysis of melt band formation by simple shear, *Geochem. Geophys. Geosyst.*, *4*(9), 8615, doi:10.1029/2002GC000499.

Spiegelman, M., and D. McKenzie (1987), Simple 2-D models for melt extraction at mid-ocean ridges and island arcs, *Earth Planet. Sci. Lett.*, *83*, 137–152.

Spiegelman, M., P. B. Kelemen, and E. Aharonov (2001), Causes and consequences of flow organization during melt transport: The reaction infiltration instability in compactible media, *J. Geophys. Res.*, *106*, 2061–2077.

Stevenson, D. J. (1989), Spontaneous small-scale melt segregation in partial melts undergoing deformation, *Geophys. Res. Lett.*, *16*, 1067–1070.

Takei, Y. (1998), Constitutive mechanical relations of solid-liquid composites in terms of grain-boundary contiguity, *J. Geophys. Res.*, *103*, 18,183–18,203.

Takei, Y. (2001), Stress-induced anisotropy of partially molten media inferred from experimental deformation of a simple binary system under acoustic monitoring, *J. Geophys. Res.*, *106*, 567–588.

Takei, Y. (2005), Deformation-induced grain boundary wetting and its effects on the acoustic and rheological properties of partially molten rock analogue, *J. Geophys. Res.*, *110*, B12203, doi:10.1029/2005JB003801.

Takei, Y., and B. K. Holtzman (2009a), Viscous constitutive relations of solid-liquid composites in terms of grain boundary contiguity: 1 Grain boundary diffusion control model, *J. Geophys. Res.*, doi:10.1029/2008JB005850, in press.

Takei, Y., and B. K. Holtzman (2009b), Viscous constitutive relations of solid-liquid composites in terms of grain boundary contiguity: 2. Compositional model for small melt fractions, *J. Geophys. Res.*, doi:10.1029/2008JB005851, in press.

Zimmerman, M. E., and D. L. Kohlstedt (2004), Rheological properties of partially molten Lherzolite, *J. Petrol.*, *45*, 275–298.

Zimmerman, M. E., S. Zhang, D. L. Kohlstedt, and S. Karato (1999), Melt distribution in mantle rocks deformed in shear, *Geophys. Res. Lett.*, *26*, 1505–1508.

B. K. Holtzman, Lamont-Doherty Earth Observatory, Earth Institute at Columbia University, 61 Route 9W, Palisades, NY 10964-1000, USA. (benh@ldeo.columbia.edu)

Y. Takei, Earthquake Research Institute, University of Tokyo, 1-1-1 Yayoi, Bunkyo-ku, Tokyo 113-0032, Japan. (ytakei@eri.u-tokyo.ac.jp)